Gastroenterology 2024;167:1183–1197

Gut Pathobiont–Derived Outer Membrane Vesicles Drive Liver Inflammation and Fibrosis in Primary Sclerosing Cholangitis–Associated Inflammatory Bowel Disease

Heidrun Dorner,[1,*] **Iris Stolzer**,[1,*] Jochen Mattner,[2,3] Sophie Kaminski,[1] Sofia Leistl,[1] Lisa-Maria Edrich,[1] Raphael Schwendner,[1] Julia Hobauer,[1] Adrian Sebald,[1] Stefanie Leikam,[1] Miguel Gonzalez Acera,[1] Miriam Düll,[1] Roland Lang,[2,3] Gerald Seidel,[4] Tatjana Seitz,[5] Claus Hellerbrand,[5] Gregor Fuhrmann,[6] Ute Distler,[7] Stefan Tenzer,[7] Phillip Eichhorn,[8] Michael Vieth,[9] Christoph Schramm,[10] Philipp Arnold,[11] Christoph Becker,[1,3,12] Carl Weidinger,[13] Britta Siegmund,[13] Raja Atreya,[1,3,12] Moritz Leppkes,[1,12] Elisabeth Naschberger,[14] Fotios Sampaziotis,[15,16,17] Peter Dietrich,[1,5] Manfred Rauh,[18] Stefan Wirtz,[1,3,12] Andreas E. Kremer,[1,12,19] Markus F. Neurath,[1,3,12] and Claudia Günther[1,3,12]

[1]Department of Medicine 1, Universitätsklinikum Erlangen and Friedrich-Alexander-Universität Erlangen-Nürnberg, Erlangen, Germany; [2]Institute of Clinical Microbiology, Immunology and Hygiene, Universitätsklinikum Erlangen and Friedrich-Alexander-Universität Erlangen-Nürnberg, Erlangen, Germany; [3]Friedrich-Alexander-Universität Erlangen-Nürnberg Profile Center Immunomedicine, Friedrich-Alexander-Universität Erlangen-Nürnberg, Erlangen, Germany; [4]Microbiology, Department of Biology, Friedrich-Alexander-Universität Erlangen-Nürnberg, Erlangen, Germany; [5]Institute of Biochemistry, Friedrich-Alexander-Universität Erlangen-Nürnberg, Erlangen, Germany; [6]Department of Biology, Pharmaceutical Biology, Friedrich-Alexander-Universität Erlangen-Nürnberg, Erlangen, Germany; [7]Institute of Immunology, University Medical Center of the Johannes-Gutenberg University, Mainz, Germany; [8]Institute of Pathology, Universitätsklinikum Erlangen and Friedrich-Alexander-Universität Erlangen-Nürnberg, Erlangen, Germany; [9]Institute of Pathology, Klinikum Bayreuth, Friedrich-Alexander-Universität Erlangen-Nürnberg, Bayreuth, Germany; [10]Department of Medicine, Martin Zeitz Center for Rare Diseases, University Medical Center Hamburg-Eppendorf, Hamburg, Germany; [11]Institute of Functional and Clinical Anatomy, Friedrich-Alexander-Universität Erlangen-Nürnberg, Erlangen, Germany; [12]Deutsches Zentrum Immuntherapie, Universitätsklinikum Erlangen, Erlangen, Germany; [13]Division of Gastroenterology, Infectiology and Rheumatology, Charité-Universitätsmedizin Berlin, corporate member of Freie Universität Berlin and Humboldt-Universität zu Berlin, Berlin, Germany; [14]Division of Molecular and Experimental Surgery, Department of Surgery, Universitätsklinikum Erlangen and Friedrich-Alexander-Universität Erlangen-Nürnberg, Erlangen, Germany; [15]Wellcome–Medical Research Council Cambridge Stem Cell Institute, Cambridge, United Kingdom; [16]Cambridge Liver Unit, Cambridge University Hospitals National Health Service Foundation Trust, Cambridge, United Kingdom; [17]Department of Medicine, University of Cambridge, Cambridge, United Kingdom; [18]Research Laboratory, Division of Pediatrics, Universitätsklinikum Erlangen and Friedrich-Alexander-Universität Erlangen-Nürnberg, Erlangen, Germany; and [19]Department of Gastroenterology and Hepatology, University Hospital Zürich, University of Zürich, Zürich, Switzerland

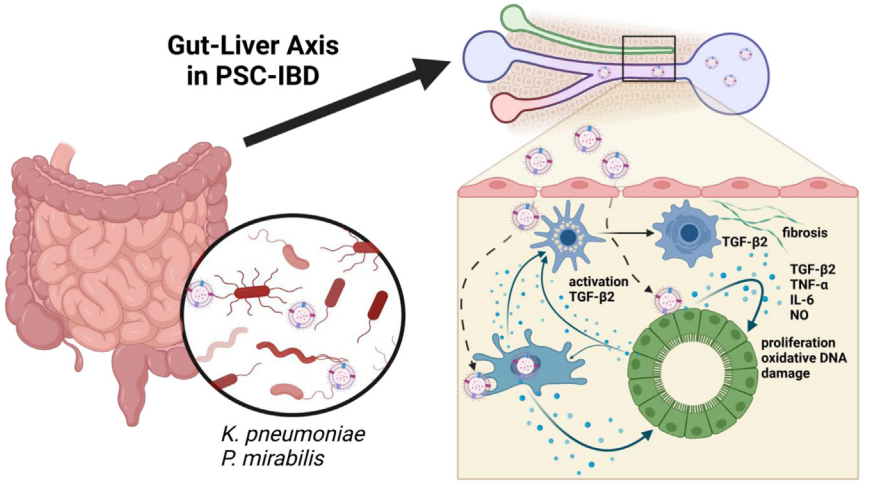

Gastroenterology

BACKGROUND & AIMS: Primary sclerosing cholangitis (PSC), often associated with inflammatory bowel disease (IBD), presents a multifactorial etiology involving genetic, immunologic, and environmental factors. Gut dysbiosis and bacterial translocation have been implicated in PSC-IBD, yet the precise mechanisms underlying their pathogenesis remain elusive. Here, we describe the role of gut pathobionts in promoting liver inflammation and fibrosis due to the release of bacterial outer membrane vesicles (OMVs). **METHODS:** Preclinical mouse models in addition to ductal organoids were used to acquire mechanistic data. A proof-of-concept study including serum and liver biopsies of a patient cohort of PSC (n = 22), PSC-IBD (n = 45), and control individuals (n = 27) was performed to detect OMVs in the systemic circulation and liver. **RESULTS:** In both preclinical model systems and in patients with PSC-IBD, the translocation of OMVs to the liver correlated with enhanced bacterial sensing and accumulation of the NLRP3 inflammasome. Using ductal organoids, we were able to precisely attribute the pro-inflammatory and pro-fibrogenic properties of OMVs to signaling pathways dependent on Toll-like receptor 4 and NLRP3–gasdermin-D. The immunostimulatory potential of OMVs could be confirmed in macrophages and hepatic stellate cells. Furthermore, when we administered gut pathobiont–derived OMVs to *Mdr2*$^{-/-}$ mice, we observed a significant enhancement in liver inflammation and fibrosis. In a translational approach, we substantiated the presence of OMVs in the systemic circulation and hepatic regions of severe fibrosis using a PSC-IBD patient cohort. **CONCLUSIONS:** This study demonstrates the contribution of gut pathobionts in releasing OMVs that traverse the mucosal barrier and, thus, promote liver inflammation and fibrosis in PSC-IBD. OMVs might represent a critical new environmental factor that interacts with other disease factors to cause inflammation and thus define potential new targets for fibrosis therapy.

Keywords: Bacterial Extracellular Vesicle; Hepatic Inflammation; PSC-IBD; Inflammasome.

WHAT YOU NEED TO KNOW

BACKGROUND AND CONTEXT

In the context of primary sclerosing cholangitis–associated inflammatory bowel disease, the gut microbiota, including pathobionts like *Klebsiella pneumoniae* and *Proteus mirabilis*, actively shapes the disease's initiation and progression, highlighting its significance in this multifactorial disorder.

NEW FINDINGS

Bacterial outer membrane vesicles released by the gut microbiota were identified as a critical new environmental factor that interacts with other disease factors to cause inflammation and fibrosis in the liver.

LIMITATIONS

Although bacterial outer membrane vesicles could be detected within the systemic circulation of patients with primary sclerosing cholangitis–associated inflammatory bowel disease, the bacterial origin of these vesicles is not entirely clear.

CLINICAL RESEARCH RELEVANCE

This study suggests that bacterial outer membrane vesicles might serve as a diagnostic marker to identify patients with primary sclerosing cholangitis with impaired barrier function and further represent a potential new target for fibrosis therapy.

BASIC RESEARCH RELEVANCE

This study identifies specific immune signaling pathways involving Toll-like receptor 4, the NLRP3 inflammasome, as well as gasdermin-D–mediated pyroptosis. These pathways are critical components of the innate immune system, working synergistically to orchestrate the host immune response to bacterial outer membrane vesicles, potentially contributing to liver inflammation and fibrosis.

HEPATOBILIARY

Primary sclerosing cholangitis (PSC) is an idiopathic, chronic cholestatic liver disease characterized by biliary inflammation, cholestasis, and multifocal bile duct strictures, and is strongly associated with inflammatory bowel disease (IBD). Although the exact etiology is not fully understood, emerging evidence suggests that the pathology is a multifactorial disorder involving genetic, immunologic, and environmental factors. Among them, gut dysbiosis and translocation of bacteria or bacterial-derived products have been highly associated with PSC. Indeed, emerging evidence indicates that not only IBD, but also PSC, is characterized by alterations in gut microbial and metabolite composition, associated with portal bacteremia and elevated endotoxin levels in cholangiocytes.[1–3] Previous clinical studies have demonstrated that PSC harbors genus-specific and species-specific alterations with an enrichment of *Klebsiella pneumoniae*, *Proteus mirabilis*, *Enterococcus gallinarum*, *Lactobacillus gasseri*, and bacteria of the genera *Veillonella* and *Fusobacterium*.[2,4,5] Functional studies provided strong evidence for a direct link between this microbial dysbiosis and liver inflammation. On a mechanistic level, it has been demonstrated that the gut pathobiont *K pneumoniae* promotes bacterial translocation, due to its pore-forming ability in the intestinal epithelium. Importantly, although these data strongly suggest a pivotal role of the gut microbiota and mucosal barrier dysfunction, no bacteria could be grown from the liver, suggesting a causal link, but pointing against a translocation of living bacteria to the liver.[2] Besides direct bacteria–host cell interaction, inter-kingdom cross-talk includes several indirect communication systems that do not require direct contact or close anatomic location. This does not

*** Authors share co-first authorship.**

Abbreviations used in this paper: **EBO, extrahepatic biliary organoid; GBP, guanylate-binding protein; GSDMD, gasdermin-D; hIBO, human-derived intrahepatic biliary organoid; HSC, hepatic stellate cell; IBD, inflammatory bowel disease; IBO, intrahepatic biliary organoid; LPS, lipopolysaccharide; mRNA, messenger RNA; MyD88, myeloid differentiation primary response 88; NF-κB, nuclear factor–κB; OmpC, outer membrane protein C; OMV, outer membrane vesicle; PSC, primary sclerosing cholangitis; TGF, transforming growth factor; TLR, Toll-like receptor.**

Most current article

0016-5085/$36.00
https://doi.org/10.1053/j.gastro.2024.06.032

only include bacterial metabolites, such as short-chain fatty acids and modified bile acids but further bacterial effector molecules, including lipopolysaccharide (LPS). Bacterial toxins and immunostimulatory byproducts are suggested to promote immune-mediated damage of hepatocytes and the biliary tree, resulting in biliary injury, cholangiocyte remodeling, and fibrosis. These effector proteins have to cross several barriers to tackle the host. Emerging evidence from our own group and others indicates that bacterial-derived extracellular vesicles are able to cross the mucosal and blood barrier to function as communication tools that modulate tissue and immune homeostasis.[6] A recent study from our laboratory found that bacterial-derived extracellular vesicles derived from the outer membrane of Gram-negative bacteria (outer membrane vesicles [OMVs]) can disseminate to distant tissue sites independent of their parental bacterium being localized in the gut lumen, and are able to transfer embodied bioactive molecules to the liver.[7] OMVs can modulate the host`s immune response by affecting both the innate and adaptive immune system. In this context, several OMVs have been found to stimulate the production of pro-inflammatory cytokines and increase the activation of immune cells, and while others can suppress the immune response and promote tolerance.[8,9] Indeed, our previous study demonstrated that biliary epithelial cells and myeloid cells recognize pathogen-associated molecular patterns present in OMVs.[7] Moreover, OMVs have been identified in a wide range of human biofluids and tissues and recently increased serum levels of LPS-positive bacterial-derived extracellular vesicles were identified in patients with IBD.[10] This strengthens the idea that OMVs are a new player along the gut–liver axis, potentially exerting multifaceted roles in the initiation and progression of PSC.

The present study was conducted to investigate the immunostimulatory potential of OMVs on liver-resident immune and epithelial cells and to test the hypothesis that these OMVs might contribute to liver inflammation and fibrosis.

Materials and Methods

Human Samples

All studies with human material were approved by the Ethics Committee (#49_16B) of the Universitätsklinikum Erlangen. The diagnosis of PSC and PSC-IBD was based on clinical, endoscopic, radiology, and histologic findings. A comprehensive description of the patient cohort is presented in Supplementary Table 1.

All other methods are described in detail in the Supplementary Material.

Results

Bacterial-Derived Outer Membrane Vesicles Target Liver-Resident Ductal Cells

To address microbe–host communication, we recently established a robust in vivo model that allows us to visualize the transfer of bioactive microbial molecules from the gut lumen to the host organism by OMVs (Figure 1*A*).[7] By taking advantage of this model system, we now observed that OMVs are able to cross the mucosal barrier to target liver-resident cells, including hepatocytes, endothelial cells, and biliary epithelial cells (Figure 1*B* and *C*). Importantly, consistent with our previous publication, we were unable to detect intact bacteria in the liver of these animals, as demonstrated by the absence of GFP-expressing *Escherichia coli* (Figure 1*B*) and fluorescence in situ hybridization with a universal bacterial probe (Eub338) (data not shown).[7] These data provide strong evidence that OMVs allow communication along the gut–liver axis.

To investigate the biodistribution of OMVs in a pathophysiological context, we stained liver cross sections from *Mdr2*$^{-/-}$ mice, a well-established mouse model for PSC, with an antibody against the outer membrane protein C (OmpC). Although previous studies described intestinal barrier dysfunction and bacterial translocation in *Mdr2*$^{-/-}$ animals on an FVB/N,[11] BALB/c,[12] or even C57BL/6[2,13] background, we could not observe signs of bacterial translocation or sensing of bacterial antigens, when mice were kept on a C57BL/6 background and housed under specific-pathogen–free conditions (Figure 1*D*, Supplementary Figure 1*A* and *B*). Because PSC is strongly associated with mucosal inflammation and clinically with IBD, we generated *Mdr2*$^{-/-}$ animals with an additional intestinal epithelial cell–specific deletion of caspase-8 (*Casp8*$^{\Delta IEC}$x*Mdr2*$^{-/-}$ animals). *Casp8*$^{\Delta}$IEC animals are widely used as a preclinical model for IBD[14–16] and previous studies from our group elucidated an altered mucosal and systemic immune response in these mice,[17] associated with mild hepatic inflammation. Both control and genetically modified strains exhibited similar rates of body weight gain up to week 18 after birth, without displaying any phenotypic alterations. Interestingly, between 20 and 30 weeks of age, *Casp8*$^{\Delta ICE}$, *Mdr2*$^{-/-}$, and *Casp8*$^{\Delta ICE}$x*Mdr2*$^{-/-}$ mice showed a notable increase in weight gain compared with control animals (Supplementary Figure 2*A*). Within this experimental group, we observed OmpC-positive signals in close proximity to the luminal side of the biliary epithelium, as well as the luminal surface of endothelial cells of the portal vein in *Casp8*$^{\Delta IEC}$x*Mdr2*$^{-/-}$ animals but not *Mdr2*$^{-/-}$ mice (Figure 1*D*). We also observed the translocation of OMVs to the liver of *Casp8*$^{\Delta ICE}$ mice, along with mild liver inflammation and fibrosis in a subset of these animals (to a similar extent as PSC is observed in IBD) (Supplementary Figure 2*B*). However, the majority of *Casp8*$^{\Delta ICE}$ mice displayed no notable changes in liver histology, or alterations in RNA expression levels (Supplementary Figure 2*B–D*).

Of particular note, current publications demonstrated the recognition of OMVs by the innate immune system via the NLRP3 inflammasome.[18] In line with this, the presence of OMVs was associated with signals for NLRP3, particularly around the biliary epithelium and hepatic vessels in these double-deficient mice, but not in *Mdr2*$^{-/-}$ animals (Figure 1*D*). This was associated with significantly increased messenger RNA (mRNA) levels of hepatic *Nlrp3*, as well as other key factors of bacterial sensing in the liver (Supplementary Figure 1*C*). Although we could detect bacterial signals in the small and large intestine, we could not observe 16S ribosomal RNA signals in the liver (Supplementary Figure 1*B*).

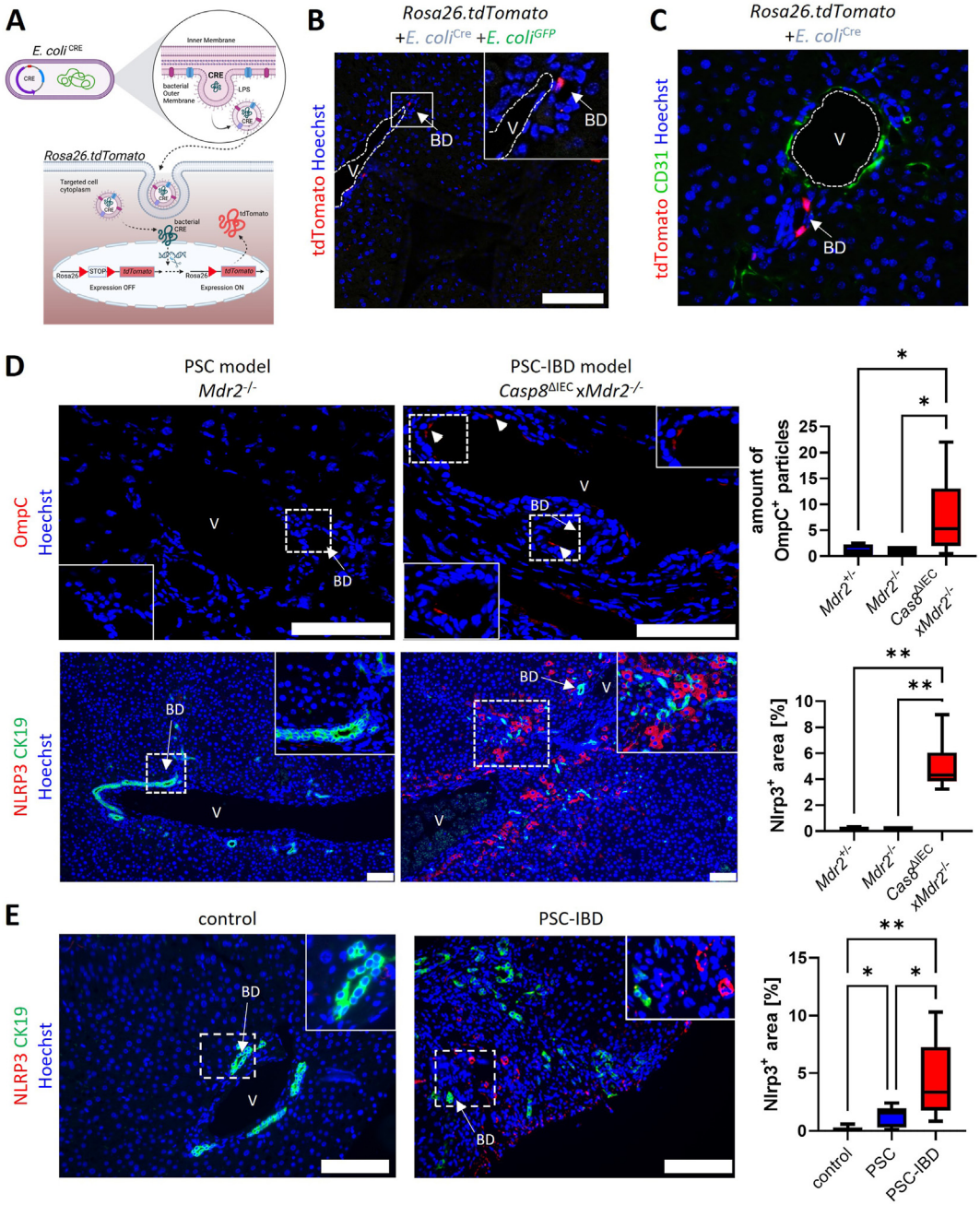

Figure 1. Translocation of OMVs to the liver is associated with NLRP3 up-regulation in PSC-IBD (*A*) Graphical depiction of the used cargo system. Host cells take up OMVs loaded with bioactive Cre, resulting in Cre-mediated removal of the *loxP*-flanked STOP cassette and induction of *tdTomato* expression. (*B, C*) Representative data derived from liver cross sections of *Rosa26.tdTomato* mice treated with either (*B*) *E coli* ^{Cre} (3×10^9) plus *E coli* ^{GFP}(3×10^9) or (*C*) only with *E coli*^{Cre} (6×10^9). Experiment was repeated 3 times with similar results. (*B*) Pictures of tdTomato-positive biliary epithelial cells (*scale bar:* 100 μm) and (*C*) cross sections additionally stained with an antibody against CD31 (*green*). (*D, E*) Mice were sacrificed at approximately 30 weeks. Experiment was repeated 3 times with similar results. (*D*) Representative *images* of liver cross sections immunohistochemically stained with antibodies against OmpC (*red*) or NLRP3 (*red*) and CK19 (*green*). *Scale bar:* 100 μm. Corresponding quantification. *Mdr2*$^{+/-}$ n $\geq$ 4; *Mdr2*$^{-/-}$ n $\geq$ 3; *Casp8*$^{\Delta IEC}$x*Mdr2*$^{-/-}$ n $\geq$ 6; statistical test: Brown-Forsythe and Welch analysis of variance with Dunnett's T3 multiple comparisons test. (*E*) Representative images of human liver biopsies stained with antibodies against NLRP3 (*red*) and CK19 (*green*). *Scale bar:* 130 μm. Corresponding quantification of NLRP3-positive area. Control n = 3, PSC n = 8, PSC-IBD, n = 12, statistical test: Brown-Forsythe and Welch analysis of variance with Dunnett's T3 multiple comparisons test. BD, bile duct; V, vessel. *$P < .05$; **$P < .01$.

In support of previous publications, our study highlights a potential association between the shuttling of bacterial-derived biomolecules via OMVs and the up-regulation of hepatic NLRP3, a factor that might trigger inflammation and fibrosis in the context of PSC-IBD. In a translational approach, we further observed a notable increase in hepatic NLRP3 protein expression in patients with PSC-IBD (Figure 1*E*). Similarly, as seen in experimental PSC-IBD, the heightened NLRP3 expression was localized in close proximity to biliary epithelial cells within periportal areas (Figure 1*D* and *E*). This observation underscores the specificity and described relevance of NLRP3 in the context of PSC-IBD.

These findings strongly suggest that impaired barrier function is associated with the transfer of microbial bioactive molecules via OMVs to the liver, which might contribute to hepatic inflammation and fibrosis.

Outer Membrane Vesicles Induce Toll-Like Receptor Activation Associated With a Pro-Inflammatory Signature

Given the high presence of OMVs in close proximity to cholangiocytes, we next investigated the immune modulatory properties of OMVs on liver-resident cells. To delineate the immunogenic potential on biliary epithelial cells, we took advantage of ductal organoids derived from the intrahepatic (IBO) and extrahepatic biliary (EBO) system (Supplementary Figure 3*A*). OMVs faithfully resemble the composition of the bacterial outer membrane and act as potent activators of Toll-like receptors (TLRs), leading to the production of pro-inflammatory cytokines and the activation of immune responses. The most important TLR for the recognition of pathogen-associated molecular patterns, that are expressed on the surface of OMVs, is TLR4, playing a crucial role in detecting lipid A component. In order to gain a deeper understanding of the interaction between OMVs and cholangiocytes, we conducted an analysis of *Tlr* expression in organoids. Specifically, we compared *Tlr* expression levels in cholangiocyte-derived organoids with those in tissue biopsies of the liver. We found that the *Tlr* expression pattern was similar between IBO and EBO and remained consistent between IBOs and liver biopsies (Supplementary Figure 3*B*).

To identify signaling pathways involved in host–microbe communication via OMVs, we characterized the transcriptional alterations that occur in IBOs subjected to OMVs derived from nonpathogenic *E coli.* Comparing the transcriptomes revealed a positive correlation between OMV exposure and pathways associated with immune recognition and host response against pathogens. In general, we observed a significant down-regulation of 61 genes and an up-regulation of 83 genes (Supplementary Figure 3*C*). Notably, OMV-challenged organoids displayed an enriched nuclear factor–κB (NF-κB), cytokine–cytokine receptor interaction, and interleukin 17 signature (Figure 2*A*). Gene ontology analysis on all differentially expressed genes further uncovered an enrichment of gene ontology terms in the biological function category associated with immune cell migration, regulation of inflammatory response, and positive regulation of defense response (Figure 2*A*). This suggests that IBOs were actively engaged in recognizing and responding to bacterial components within OMVs, which was further supported by an altered *Tlr* expression pattern (Supplementary Figure 3*D*). Interestingly, KEGG pathway analysis of the differentially expressed genes identified several significantly enriched terms related to inflammation, including genes involved in T-helper 17 cell differentiation, and tumor necrosis factor (TNF) signaling (Figure 2*A*, Supplementary Figure 3*E*).

In summary, these findings underscore the dynamic of IBOs' responses to OMVs, offering valuable insights into how the ductal compartment recognizes and interacts with bacterial-derived vesicles.

Outer Membrane Vesicles Mediate a Pro-Inflammatory Response and Disruption of Ductal Homeostasis Through Gasdermin D

The TLR–myeloid differentiation primary response 88 (MyD88) signaling pathway is a crucial player in innate immune signaling and the cellular response toward microbes associated with the activation of the NF-κB pathway. Indeed, recognition of OMVs by organoids leads to an increase of NF-κB target genes (Figure 2*B*). After demonstrating that cholangiocytes recognize and respond to OMVs, we next aimed to explore whether these vesicles impact biliary epithelial cell homeostasis. Thus, we conducted live cell imaging to assess the viability of organoids over an extended period after the recognition of OMVs. Exposure to OMVs resulted in a significant increase in organoid size starting 24 hours after treatment (Figure 2*C* and *D*), which was accompanied by an up-regulation in the mRNA expression of the proliferation marker *Mki67* (Figure 2*E*). Intriguingly, consistent with these in vitro findings, we also noted a significantly enhanced abundance of hepatic *Mki67* transcripts in $Casp8^{\Delta IEC}$x$Mdr2^{-/-}$ mice compared with $Mdr2^{-/-}$ single knockout animals (Figure 2*F*). Notably, we further detected pronounced Ki-67 immunostaining, particularly within the biliary epithelium of $Casp8^{\Delta IEC}$x$Mdr2^{-/-}$ mice (Figure 2*G*). Importantly, prolonged exposure to OMVs led to a decline in organoid viability (Figure 2*C* and *D*).

Consistent with our observation of increased cell death in response to OMVs, we conducted an in-depth analysis of mRNA expression patterns, particularly focusing on key factors associated with cell death. Notably, we observed a significant increase in mRNA expression of key factors for pyroptotic cell death, while genes linked to apoptotic cell death or necroptosis remained largely unchanged. In this context, gasdermin-D (*Gsdmd*) was among the top identified genes (Figure 2*H* and *I*). GSDMD is the principal executor of pyroptosis, a type of programmed cell death that is activated by the inflammasome and is essential for the host response to gram-negative bacteria.[19] Given the importance of GSDMD-mediated pyroptosis in intra- and extracellular killing of bacteria, we found that exposure of *Gsdmd*-deficient organoids to OMVs did not result in an increase in organoid size or cytotoxicity (Figure 2*J* and *K*).

These data strongly suggest that GSDMD mediates the toxic response of biliary epithelial cells to OMVs.

Lipopolysaccharide-Sensing on the Surface of Outer Membrane Vesicles Contributes to Gasdermin-D–Dependent Pyroptosis in Ductal Organoids

Intracellular LPS triggers inflammatory caspases, such as caspase-11/4, leading to GSDMD-dependent pyroptosis.[19] To test whether recognition of LPS on the surface of OMVs is necessary for GSDMD-mediated pyroptosis, we performed experiments using OMVs isolated from ClearColi BL21 (Biosearch Technologies), an *E coli* strain with a modified LPS lacking the outer membrane agonists for TLR4/MD-2 activation (Figure 3*A*). Characterization of vesicles isolated

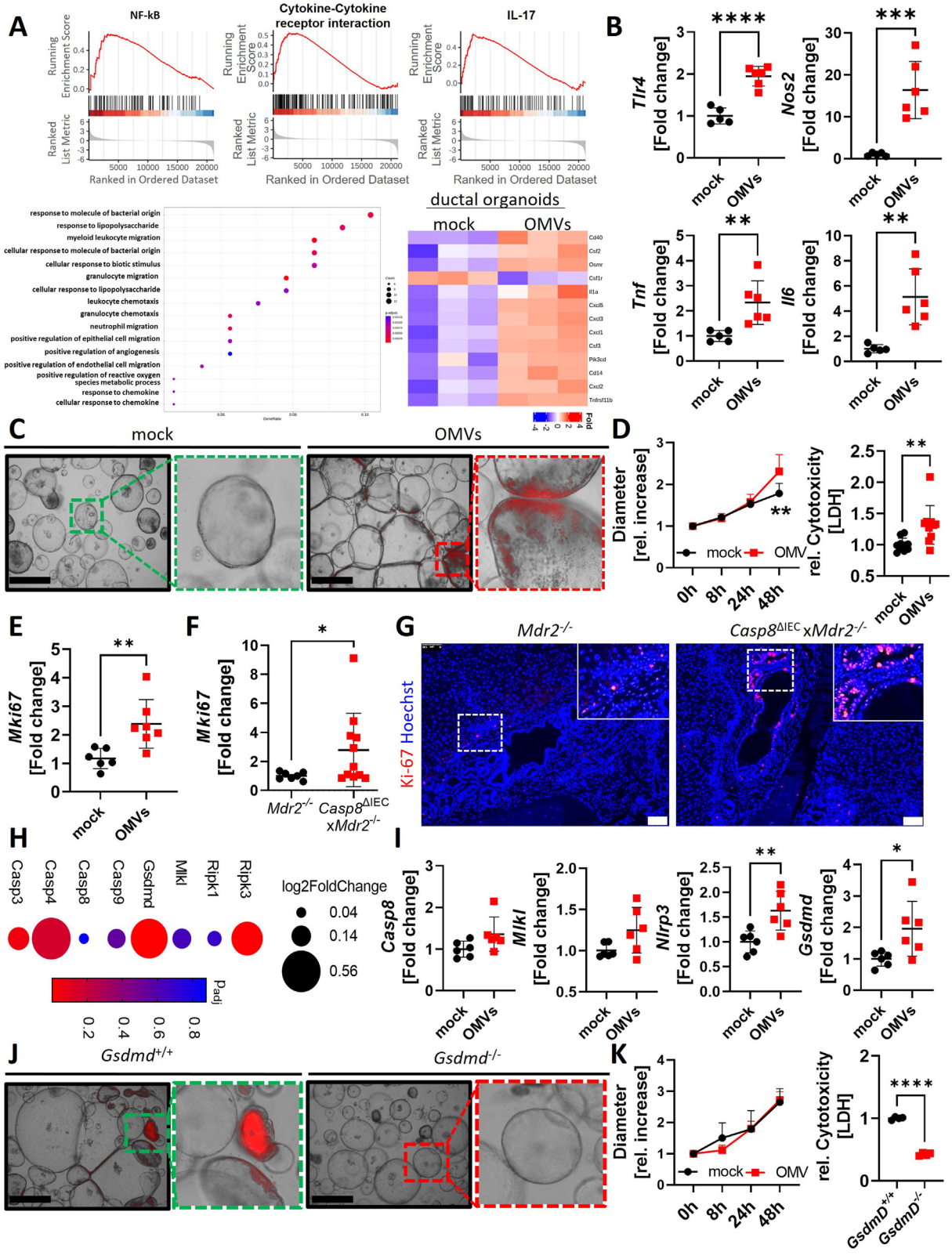

from ClearColi demonstrated that OMVs from this bacterial strain induced less NF-κB activation in HEK reporter cells expressing TLR4 (Figure 3*B*) and also mediated reduced NF-κB target gene expression in organoids (Figure 3*C*). These OMVs failed to transcriptionally up-regulate *Gsdmd* and *Casp11* and to induce cell death, suggesting that biliary pyroptosis requires sensing of LPS on the surface of OMVs (Figure 3*C*–*E*). Interestingly, bulk mRNA-sequencing data revealed that cholangiocytes respond to OMVs derived from ClearColi independent of LPS. *Defense response to bacteria* was the most prominent gene ontology term and a relevant number of genes were differentially regulated by the treatment of IBOs with these OMVs (Figure 3*F*).

These findings suggest that LPS is one of the key components of OMVs that contributes to cellular toxicity, although other membrane or vesicular components may also play a role.

Outer Membrane Vesicles Trigger Pro-Fibrotic Marker Gene Expression in Ductal Organoids and Liver Parenchymal Cells

In addition to their role in releasing cytokines and chemokines that contribute to inflammation, activated cholangiocytes have been demonstrated to directly impact the biology of myofibroblasts via transforming growth factor (TGF)-β. Our initial experiments revealed that the exposure of organoids to OMVs resulted in an explicit and rapid up-regulation of *Tgfb1* and *Tgfb2* mRNA expression (Supplementary Figure 4*A*), which was supported by our RNA-sequencing data. These findings prompted us to further investigate the molecular mechanisms that regulate *Tgfb2* gene transcription in biliary epithelial cells. We observed that GSDMD mediates the cytotoxicity of OMVs. However, the absence of *Gsdmd* did not prevent the substantial increase in *Tgfb2* mRNA expression after OMV exposure, but rather altered the inflammatory response. We further found that TLR-MyD88 signaling plays a crucial role in the transcriptional regulation of the NF-κB–mediated pro-inflammatory response. However, the lack of *Myd88* only hampered *Tgfb2* transcription in organoids (Supplementary Figure 4*B*).

Building on our observation of *Tgfb2* expression in organoids after OMV exposure, we next sought to investigate whether OMVs could elicit a pro-fibrotic response in human hepatic stellate cells (HSCs).[20] OMVs did not affect HSC viability (Supplementary Figure 4*C*), but induced a pro-inflammatory response. Interestingly, our data demonstrated that LPS on the surface of OMV also promotes the expression of genes relevant for NLRP3 inflammasome in HSZ-B cells (Supplementary Figure 4*D*).

Besides cholangiocytes, macrophages can contribute to the activation of HSCs, leading to collagen production and fibrotic tissue remodeling. Henceforth, we next performed in vitro experiments to explore OMVs' immunogenic capabilities when encountered by macrophages. The presence of LPS on the surface of OMVs predominantly accounted for the pro-inflammatory gene expression pattern exhibited by macrophages (Supplementary Figure 4*E*). Intriguingly, OMVs sourced from ClearColi, despite their nonpathogenic nature, also evoked a significant up-regulation in the mRNA expression of genes closely linked with bacterial sensing and inflammatory responses (Supplementary Figure 4*E*). This observation suggests a broader capacity of OMVs, extending beyond their LPS content, to stimulate immune and inflammatory pathways within macrophages. Consistent with our hypothesis, our in vivo experiments using the *Casp8*$^{\Delta IEC}$x*Mdr2*$^{-/-}$ mouse model identified a population of nonparenchymal cells that coexpressed α–smooth muscle actin and NLRP3, indicating that HSCs respond to OMVs in the context of experimental PSC (Supplementary Figure 5*A* and *C*). In addition, we detected NLRP3 up-regulation in F4/80^{+} cells, a major macrophage marker with robust expression observed in Kupffer cells located in close proximity to the biliary epithelium within the portal triad (Supplementary Figure 5*B*) comparable with the localization of detected OMVs (Supplementary Figure 5*D*).

Figure 2. OMVs trigger pro-inflammatory response and biliary epithelial cell homeostasis disruption via GSDMD. (*A*) Bulk RNA sequencing data of murine IBO stimulated with OMVs derived from *E coli* BL21 (8.6×10^8 particles/mL) or mock treated for 8 hours. Gene set enrichment analysis plot of indicated pathways enriched in OMV exposed ductal organoids, top gene ontology terms and *heat map* of differentially expressed genes. (*B*) Gene transcription analysis of IBOs stimulated with OMVs (8.6×10^8 particles/mL) or mock treated for 8 hours. mRNA expression was normalized to *Rpl37a.* mock n = 5; OMVs n = 6; statistical test: unpaired *t* test. (*C–E*) Murine IBO stimulated with OMVs (1×10^9 particles/mL) or mock treated for 72 hours. (*C*) Representative *images* of organoids stained with propidium iodide (PI) (*red*, dead cells). (*D*) Corresponding analysis of growth by the relative increase of the size diameter (n = 4 per group; statistical test: 2-way analysis of variance with Šídák's multiple comparisons test) and relative cytotoxicity measured by lactate dehydrogenase (LDH) release (n = 10 per group; statistical test: unpaired *t* test) and (*E*) gene transcription analysis (mock n = 6; OMVs n = 7; statistical test: unpaired *t* test). (*F, G*) Mice were sacrificed at approximately 30 weeks. Pooled data of independent experiments. *Mdr2*$^{-/-}$ n = 7; *Casp8*$^{\Delta IEC}$x*Mdr2*$^{-/-}$ n = 11; statistical test: Welch's *t* test. (*F*) Gene transcription analysis of murine liver tissue normalized to *Hprt.* (*G*) Representative *images* of liver cross sections stained with antibodies against Ki-67 (*red*). *Scale bar:* 100 μm. (*H, I*) Murine IBO were stimulated with OMVs (8.6×10^8 particles/mL) or mock treated for 8 hours. (*H*) Bulk RNA-sequencing data. Selected genes associated with cell death are displayed. (*I*) mRNA expression normalized to *Rpl37a*. mock n = 6; OMVs n = 6; statistical test: unpaired *t* test. (*J*) Control and *Gsdmd*-deficient IBO were stimulated with OMVs (8×10^9 particles/mL) or mock treated for 72 hours. Representative *images* stained with PI (*red*, dead cells). (*K*) Corresponding analysis of growth by relative increase in size (n = 4 per group; statistical test: 2-way analysis of variance with Šídák's multiple comparisons test) and relative cytotoxicity measured by LDH release (n = 4 per group; statistical test: unpaired *t* test). **P* < . 05; ***P* < .01; ****P* < .001; *****P* < .0001.

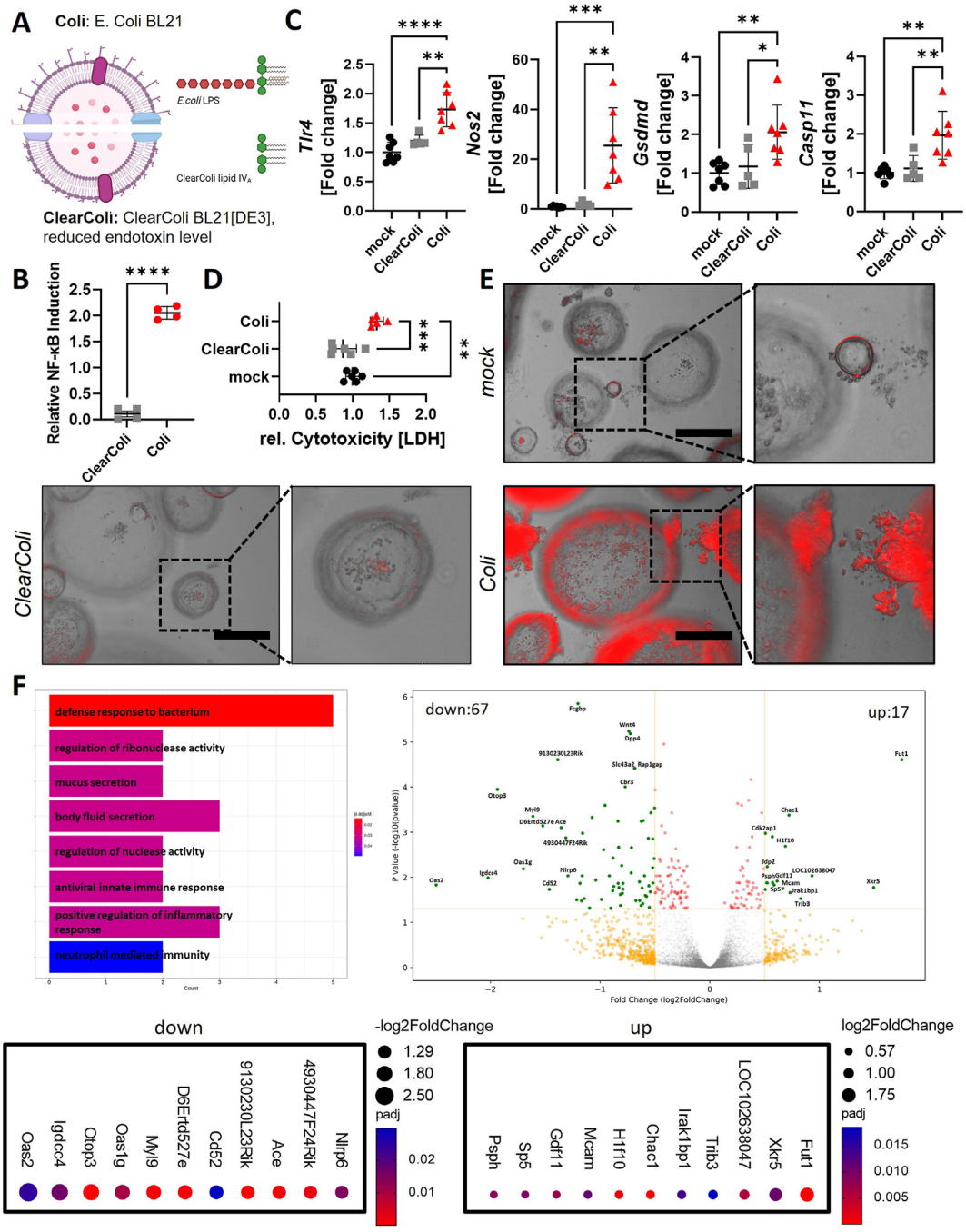

Figure 3. LPS-independent sensing of OMVs by ductal epithelial cells. (*A*) OMVs derived from *E coli* BL21 or genetically modified ClearColi *E coli* (Biosearch Technologies). (*B*) Relative NF-κB induction in HEK-Blue reporter cells (n = 4 per group; statistical test: unpaired *t* test). (*C–E*) Murine IBO were stimulated with OMVs (8.6×10^8 particles/mL) or mock treated. (*C*) Gene expression analysis (after 8 hours) normalized to *Rpl37a*. n ≥ 5 per group; statistical test: ordinary 1-way analysis of variance (ANOVA) with Tukey's multiple comparisons test. (*E*) Representative *images* of PI (*red*, dead cells) staining and (*D*) relative cytotoxicity measured by lactate dehydrogenase (LDH) release after 72 hours. n ≥ 5 per group; statistical test: ordinary 1-way ANOVA with Tukey's multiple comparisons test. (*F*) Bulk RNA-sequencing data of murine IBO stimulated with OMVs derived from ClearColi *E coli* BL21 (8.6×10^8 particles/mL) or mock treated for 8 hours. Top gene ontology terms, *volcano plot*, and top up-/down-regulated genes. *$P < .05$; **$P < .01$; ***$P < .001$; ****$P < .0001$.

In summary both macrophages and cholangiocytes produce pro-inflammatory cytokines after OMV recognition, but their contribution to HSC activation and liver fibrosis may vary based on the type and stage of liver disease.

Translocation of Outer Membrane Vesicles Is Associated With Exacerbated Hepatic Inflammation and Fibrosis

Our mechanistic data so far suggest that OMVs represent a critical new environmental factor that may play a

significant role in the development of liver inflammation and fibrosis. Our findings further indicate that OMVs activate biliary epithelial cells, macrophages and HSCs.

To functionally test this in vivo, we examined liver inflammation and fibrosis in *Casp8*$^{\Delta IEC}$x*Mdr2*$^{-/-}$ animals, as we have shown enhanced translocation of OMVs across the gut–liver axis in these animals (Figure 1). In line with our hypothesis, liver histology of these mice displayed severe periductular inflammation and fibrosis, including onion-shaped periportal fibrosis, typical histologic features observed in the liver of PSC-IBD patients (Figure 4*A*). Sirius Red and anti–α-smooth muscle actin staining visualized HSC activation and concomitant aggressive collagen deposition around the hepatic vasculature and the bile duct system (Figure 4*A* and *B*, Supplementary Figure 5*A*, *E*, and *F*). In line with these observations, these mice displayed enhanced collagen deposition, as well as increased mRNA expression of fibrosis-related genes (Figure 4*C* and Supplementary 5*G*). We also observed a significant increase in the expression of various macrophage markers, indicating an increase in the number and activation of macrophages (Figure 4*C*).

Immune cell infiltration is a central pathogenic feature of acute and chronic liver injury. Immunohistochemical staining revealed pronounced leukocyte infiltration, characterized by a high number of CD45^{+} and CD4^{+} cells within the portal field of *Casp8*$^{\Delta IEC}$x*Mdr2*$^{-/-}$ mice compared with *Mdr2*$^{-/-}$ mice. These inflammatory cell clusters further contained a massive number of Kupffer cells (F4/80^{+} cells), further supporting an involvement of the innate and adaptive immune system in response to OMV-induced liver injury (Figure 4*D*).

In addition to our profiling, we expanded our investigation to characterize the bile acid profile in the serum of these animals. Our findings are consistent with the established use of *Mdr2*$^{-/-}$ mice as a cholestatic mouse model, as the bile acid composition in *Mdr2*$^{-/-}$ animals exhibited hallmark features consistent with cholestasis. In contrast, the double-deficient mice did not exhibit the typical cholestatic bile acid profile. This discrepancy underscores pronounced phenotypical differences between these 2 model systems, further highlighting the significance of our findings in elucidating the mechanistic underpinnings of cholestatic disorders (Supplementary Figure 5*H*).

In summary, using a novel mouse model for PSC-IBD, we have recognized an association between clinical manifestations and the presence of OMVs within the liver of these animals. Our findings do not only underscore the relevance and fidelity of the *Casp8*$^{\Delta IEC}$x*Mdr2*$^{-/-}$ mouse model in recapitulating key aspects of human PSC-IBD, but also highlight the potential role of OMVs in driving or exacerbating the disease's pathogenesis in both mice and humans.

Outer Membrane Vesicles Derived From Gut Pathobionts Trigger Inflammation and Fibrosis in Mdr2-Deficient Mice

Based on our findings that OMVs can trigger inflammation and fibrosis in vitro, we aimed to investigate the in vivo effects of OMVs. Therefore, we challenged *Mdr2*$^{-/-}$ mice with pathogenic OMVs derived from *K pneumoniae* to impair the barrier function, followed by administration of OMVs isolated from *P mirabilis* (Figure 5*A*). Two weeks after the administration of OMVs, we observed notable alterations within the liver tissue, with *Mdr2*$^{-/-}$ mice showing an increase in liver/body ratio (Figure 5*B*). Concurrently, these mice exhibited a substantial accumulation of inflammatory cells surrounding the ductal epithelium, concomitant with early indications of periportal fibrosis (Figure 5*C* and *D*). In addition, there was a noteworthy increase of pro-inflammatory and pro-fibrotic marker gene expression (Figure 5*E*). Interestingly, the pathophysiological patterns induced by OMVs closely mirrored those observed in *Casp8*$^{\Delta IEC}$x*Mdr2*$^{-/-}$ mice, hinting towards a potential role for regulated necrosis in facilitating the translocation of OMVs in these animals (Figure 5*A*–*D*). To ascertain whether this effect was associated with bacterial sensing, as observed in *Casp8*$^{\Delta IEC}$x*Mdr2*$^{-/-}$ mice and patients with PSC-IBD, liver cross sections were stained with an antibody against NLRP3 (Figure 5*F*). Consistent with our previous data, we did not observe intact bacteria, but we did observe robust signals for NLRP3, particularly within immune cell aggregates (Figure 5*F*, Supplementary 6*A*). Crucially, no pathophysiological alterations, such as inflammatory infiltrates or signs of impaired barrier function, were evident in the colon of these animals (Supplementary Figure 6*B*). This observation strongly suggests that hepatic inflammation appears to operate independent from intestinal inflammation, once OMVs have breached the intestinal barrier.

These changes collectively point toward a dynamic response within the liver tissue after OMV exposure, which is suggestive of heightened inflammation and a pro-fibrotic milieu.

Pronounced Level of NLRP3 in Human PSC-IBD Is Associated With an Influx of Outer Membrane Vesicles

Emerging research has shed light on the potential involvement of the translocation of microbial products from the gut to the liver in the development of PSC. This complex process entails the migration of bacterial components across the gut barrier and into the systemic circulation, where they can be recognized by the innate immune system, followed by a pro-inflammatory response in the liver. Interestingly, recent studies have linked the NLRP3 inflammasome to the pathogenesis of PSC in this context.[11] Despite the observed bacterial sensing and increase of NLRP3 (Figure 1), we were unable to detect the translocation of intact bacteria into the liver of patients with PSC-IBD (Figure 6*A*). However, we observed OMVs in these patients. In line with our data derived from the preclinical model system, OmpC staining revealed positive signals in close proximity to NLRP3-expressing cells, particularly around the ductal epithelium (Figure 6*A* and *B*). Moreover, our experimental data demonstrated that recognition of OMVs was associated with an increase in GSDMD expression, a finding that we translated and confirmed by staining human liver samples for

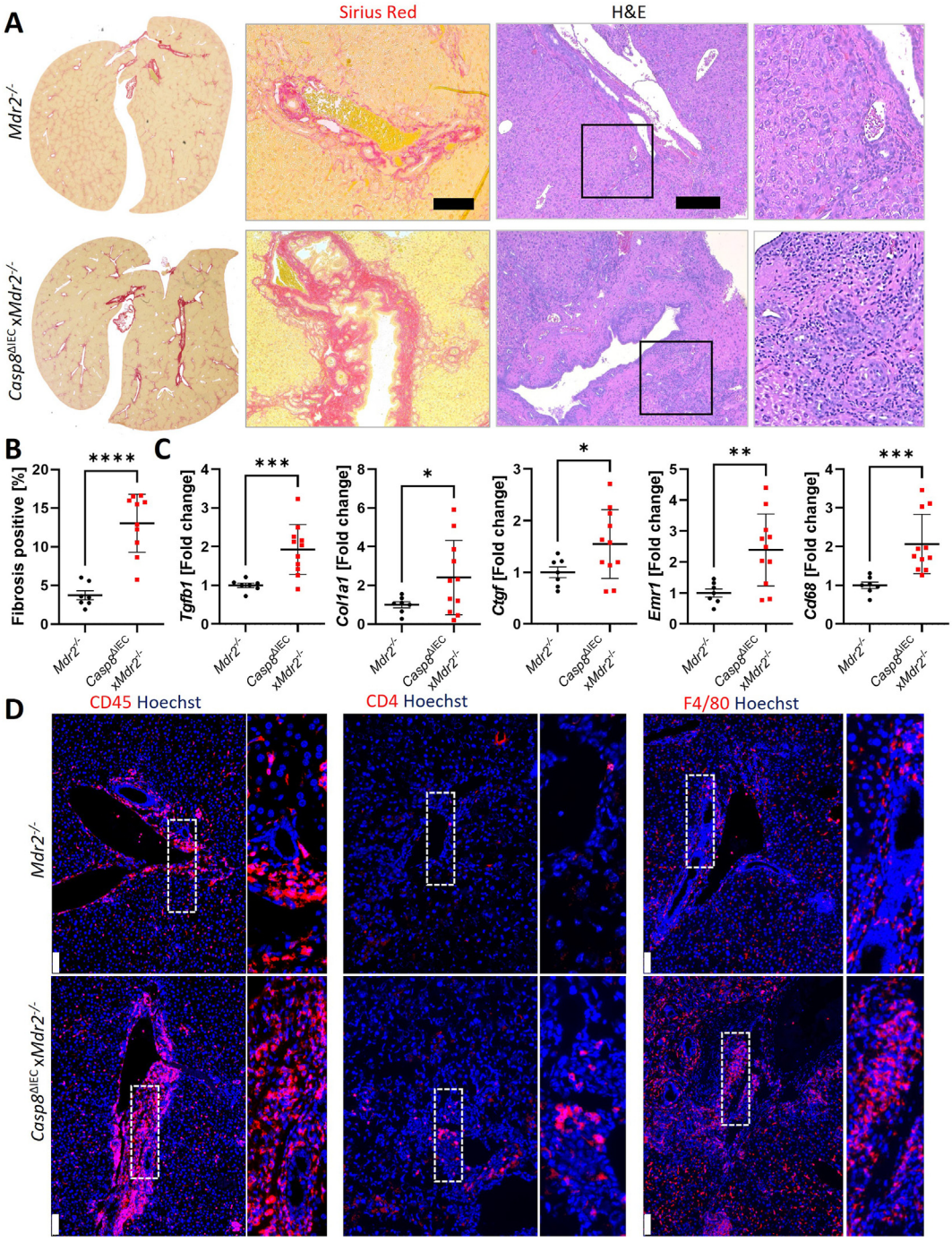

Figure 4. *Casp8*$^{\Delta IEC}$x*Mdr2*$^{-/-}$ animals as novel model for PSC-IBD. Mice were sacrificed at approximately 35 weeks. Experiment was repeated 3 times with similar results. Pooled data of individual experiments. (*A*) Representative images of liver cross sections stained with hematoxylin and eosin or Sirius Red (*scale bar:* 100 μm) and (*B*) corresponding quantification. *Mdr2*$^{-/-}$ n = 7; *Casp8*$^{\Delta IEC}$x*Mdr2*$^{-/-}$ n = 10; statistical test: Welch's *t* test. (*C*) Hepatic mRNA expression normalized to *Rpl37a*. *Mdr2*$^{-/-}$ n = 7; *Casp8*$^{\Delta IEC}$x*Mdr2*$^{-/-}$ n = 11; statistical test: Welch's *t* test. (*D*) Representative *images* of liver cross sections stained with antibodies against CD45, CD4, or F4/80 (*red*). *Scale bar:* 100 μm. *$P < .05$; **$P < .01$; ***$P < .001$; ****$P < .0001$.

GSDMD (Figure 6*A*). Interestingly, we observed a strong enrichment of GSDMD in biliary epithelial cells, but also other liver-resident cell populations, particularly in areas of severe inflammation and fibrosis within the portal field (Figure 6*A*). In addition, we noted an increase in IL-1β production around the portal vein and ductal epithelium in patients with PSC-IBD, providing further evidence that OMVs may contribute to hepatic inflammation in these patients (Figure 6*A*).

LPS-induced pyroptosis relies on TLR4-TRIF signaling-induced type I interferon production and guanylate-binding protein (GBP) action, which can directly bind LPS, followed by activation of caspase-11/4 to cleave GSDMD.[19] Remarkably, in accordance with these mechanistic

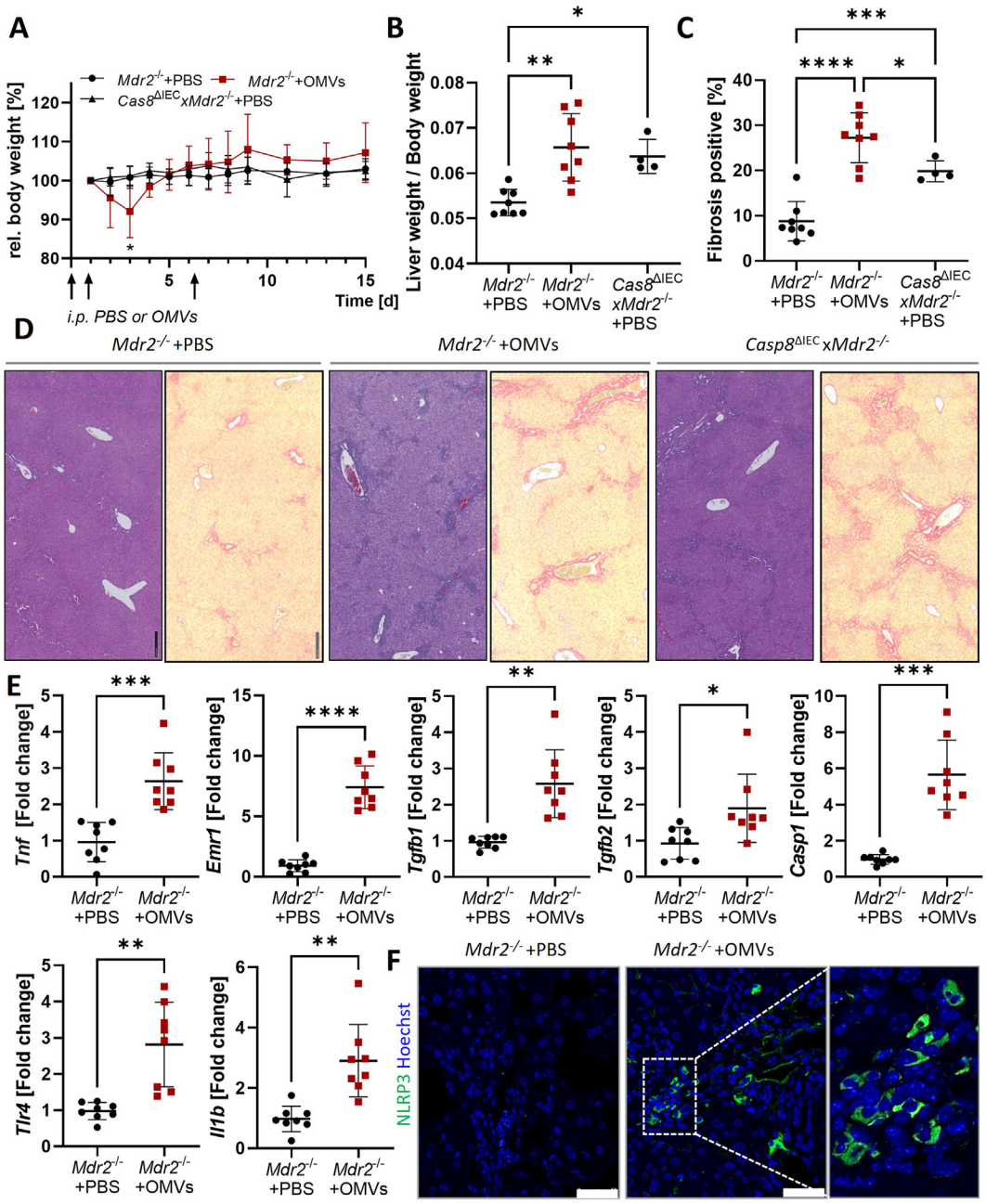

Figure 5. Gut pathobiont–derived OMVs exacerbate hepatic inflammation and fibrosis in *Mdr2*$^{-/-}$ mice. *Mdr2*$^{-/-}$ mice (age approximately 15 weeks) were injected intraperitoneally with phosphate-buffered saline (PBS) (mock) or OMVs derived from pathogenic bacteria. Day 1: *K pneumonia* (1×10^9 particles in 100 μL PBS); day 2: *P mirabilis* (2×10^9 particles in 100 μL PBS); day 8: *P mirabilis* (1×10^9 particles in 100 μL PBS). As control *Casp8*$^{\Delta IEC}$x*Mdr2*$^{-/-}$ were equally mock treated. Experiment was repeated 3 times with similar results and pooled data were displayed. *Mdr2*$^{-/-}$+PBS n = 8; *Mdr2*$^{-/-}$+OMVs n = 8, *Casp8*$^{\Delta IEC}$x*Mdr2*$^{-/-}$+PBS n = 4. *(A)* Relative body weight and (*B*) liver/body weight ratio (Brown-Forsythe and Welch analysis of variance (ANOVA) with Dunnett's T3 multiple comparisons test). (*C, D*) Representative *images* of liver cross sections stained with hematoxylin and eosin or Sirius Red (*scale bar*: 200 μm) and corresponding quantification (Brown-Forsythe and Welch ANOVA with Dunnett's T3 multiple comparisons test). (*E*) Hepatic mRNA expression normalized to *Rpl37a.* Statistical test: Welch's *t* test. (*F*) Representative *images* of liver cross sections stained with antibodies against NLRP3 (*green*). *Scale bar:* 50 μm. *$P < .05$; **$P < .01$; ***$P < .001$; ****$P < .0001$.

insights, we observed an elevated expression of GBP1 protein in patient biopsies diagnosed with PSC-IBD, as well as RNA expression in hepatic stellate cells (*GBP1*) and in macrophages (*Gbp2*) in response to OMVs (Supplementary Figure 4*D* and *E* and 7*C*).

Intriguingly, *Casp8*$^{\Delta IEC}$ mice, which were used to mimic IBD in the *Mdr2*-background, were initially characterized by MLKL-mediated cell death in the intestinal epithelium,[15,17] suggesting that regulated necrosis might contribute to the translocation of OMVs in *Casp8*$^{\Delta IEC}$x*Mdr2*$^{-/-}$ mice. In line

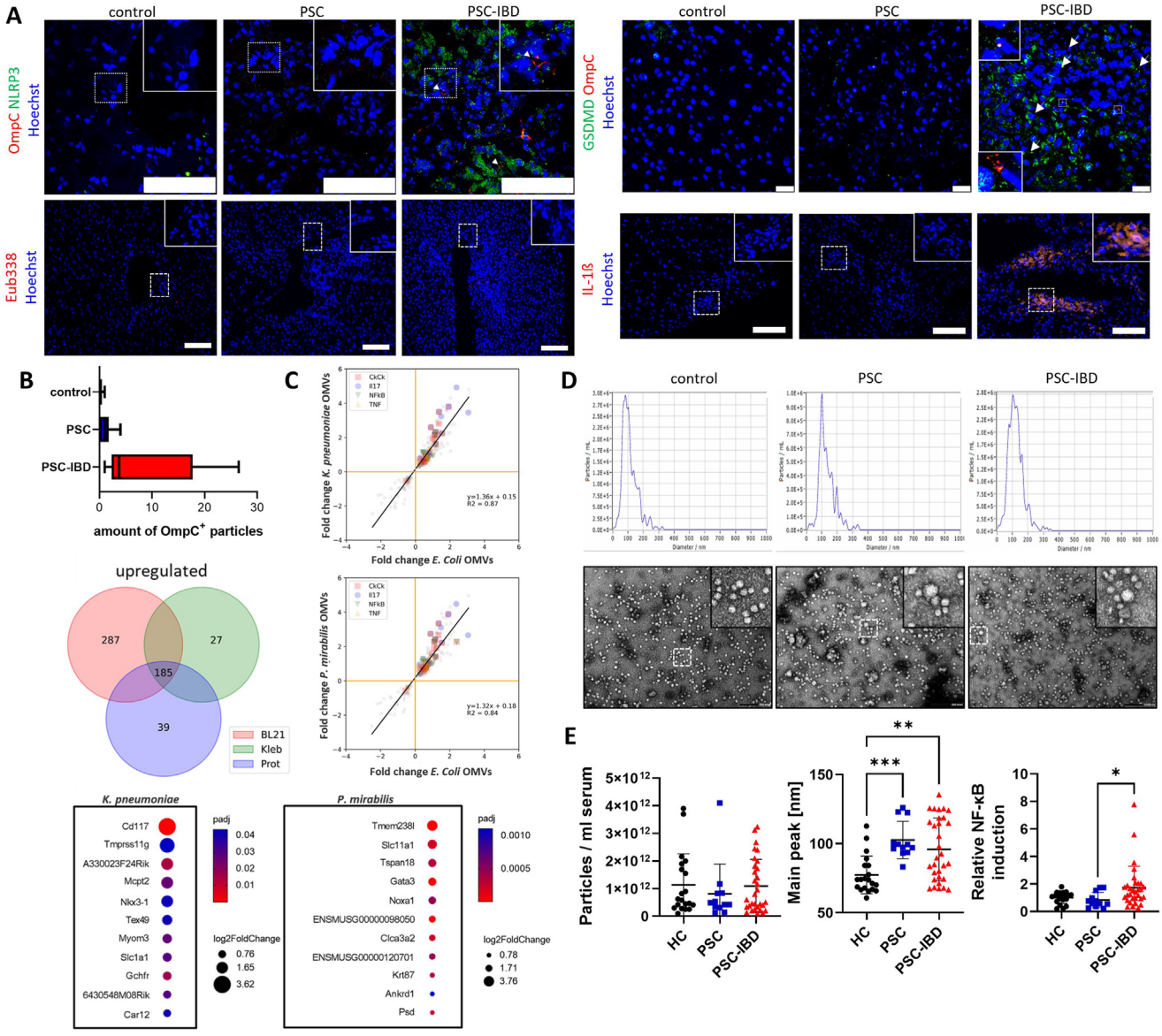

Figure 6. NLRP3 activation in human PSC-IBD correlates with OMV influx. (*A*) Representative *images* of human liver biopsy stained with antibodies against OmpC (*red*) and NLRP3 (*green*) or fluorescence in situ hybridization using a universal eubacterial probe *(red)*, *scale bar:* 100 μm or with antibodies against GSDMD (*green*) and OmpC (*red*) (*scale bar:* 250 μm), or IL-1β (*red*, *scale bar:* 250 μm). (*B*) Quantification of OmpC-positive particles. Control n = 3, PSC n = 6, PSC-IBD, n = 8, statistical test: Brown-Forsythe and Welch analysis of variance (ANOVA) with Dunnett's T3 multiple comparisons test. (*C*) Bulk RNA-sequencing analysis of ductal organoids exposed to *E coli*–derived OMVs or OMVs generated from gut pathobionts (8.6×10^8 particles/mL), stimulated for 8 hours. (*D*) Representative nanoparticle tracking analysis (NTA) and transmission electron microscopy *pictures* of patient-derived EVs. (*E*) NTA results and relative NF-κB induction in HEK-Blue reporter cells. Healthy control n = 20, PSC n = 12, PSC-IBD n = 31, statistical test: Brown-Forsythe and Welch ANOVA with Dunnett's T3 multiple comparisons test. *$P < .05$; **$P < .01$; ***$P < .001$.

with this, our recent analysis of the transcriptional profile of patients with PSC-IBD in the gut displayed alterations in the expression of proteins involved in the paracellular permeability and a notable significant increase in central cell death regulators, such as *Caspase-8* and *MLKL*, suggesting an increase in regulated cell death (Supplementary Figure 7*A*). To investigate this further, we examined patients with PSC-IBD for epithelial cell death by staining for the general cell death marker terminal deoxynucleotidyl transferase–mediated deoxyuridine triphosphate nick-end labeling (TUNEL). Consistent with the mRNA data, we found areas of severe epithelial cell death within the intestinal epithelium. These epithelial cells also stained positive for the necroptosis marker MLKL, but negative for caspase-3 activation, indicating a pro-inflammatory form of cell death (Supplementary Figure 7*B*).

To investigate the impact of OMVs derived from PSC-associated gut pathobionts on human biliary epithelial homeostasis, human ductal organoids were generated from the intrahepatic (hIBO) and extrahepatic biliary tract. After 3

weeks of isolation, clean organoid cultures were successfully established, and *TLR* expression was initially investigated (Supplementary Figure 8*A* and *B*). Although no transcripts for *TLR4* were detected under steady-state conditions, *TLR-2, -3*, and *-6*, as well as *MYD88* and *TRIF*, were expressed in all cultures (Supplementary Figure 8*B*). Interestingly, compared with human EBOs, *TLR3* was expressed significantly higher in hIBOs. After this initial characterization, we exposed hIBOs to OMVs isolated from gut pathobionts or nonpathogenic *E coli*. Interestingly, among these, only OMVs derived from *P mirabilis* induced a significant increase of *TLR4* and *TGFB2* mRNA expression in human organoids (Supplementary Figure 8*C*). To gain a more comprehensive understanding of their immunostimulatory potential, we conducted an in-depth analysis of the transcriptional profiles within organoids after exposure to pathogenic OMVs. Interestingly, both the pathogenic and nonpathogenic OMV populations exhibited the capacity to trigger signaling pathways associated with interleukin 17 and inflammation, albeit to a significantly greater extent (Figure 6*C*). Our analysis revealed a set of 185 genes that were consistently activated in the host immune response against all 3 OMV cohorts, encompassing pathways associated with infectious as well as autoimmune diseases. Although this common molecular fingerprint was identified, it is noteworthy that *E coli* OMVs evoked a broader yet comparatively weaker response compared with the pathogenic OMVs. Consequently, it became evident that both pathogenic OMV populations also triggered unique, species-specific immune responses, indicating the complexity and specificity of the host's reaction to these distinct pathogenic stimuli (Figure 6*C*, Supplementary Figure 8*D*). This suggests a nuanced interplay between the host and different types of OMVs, with potential implications for our understanding of the impact of the gut microbiota on cholestatic liver diseases.

Together, these findings suggest that OMVs may play a crucial role in triggering GSDMD-dependent cell death and NLRP3 inflammasome activation in patients with PSC-IBD. By targeting liver-resident cell populations, including biliary epithelial cells, OMVs could potentially exacerbate inflammation and liver damage in patients with PSC-IBD.

Finally, in a translational proof-of-concept study, we investigated whether the presence and amount of OMVs in the systemic circulation was associated with PSC-IBD. To assess the presence of OMVs in human serum, we conducted a comprehensive analysis comparing the quantity, size, and origin of extracellular vesicles in a patient cohort including control subjects, patients with PSC, and patients with PSC-IBD. Patient selection adhered to established exclusion criteria, which aligned with current guidelines (Supplementary Table 1).

Extracellular vesicles were isolated from serum samples and characterized using nanoparticle tracking analysis and transmission electron microscopy techniques. Importantly, transmission electron microscopy (Figure 6*D*) and western blot (data not shown) analyses indicated the successful enrichment of extracellular vesicles from serum samples. Notably, the quantified number of particles remained comparable across all patient groups. However, both patients with PSC and patients with PSC-IBD exhibited a significantly increased particle size (Figure 6*E*).

Consistent with our hypothesis, extracellular vesicles derived from patients with PSC-IBD induced a heightened activation of NF-κB in HEK reporter cells compared with vesicles from healthy controls, and significantly more than the extracellular vesicles from patients with PSC (Figure 6*E*). These data suggest that although LPS was not detected bound to extracellular vesicles in healthy controls and patients with PSC, patients with PSC-IBD displayed elevated levels of LPS-positive extracellular vesicles in their circulation. These findings point toward the potential of OMVs and their LPS content as promising diagnostic markers for PSC-IBD, underlining the clinical relevance of our study.

Overall, the results suggest that circulating OMVs may contribute to hepatic inflammation, which could be an important factor in the pathogenesis of liver disease. These findings highlight the importance of understanding the role of OMVs in the gut–liver axis and suggest that strategies targeting OMVs may be a promising therapeutic approach for treating liver disease.

Discussion

In our study, we combined preclinical mouse models with ductal organoids to visualize and gain deeper insights into host–microbe communication along the gut–liver axis in the context of cholestatic liver diseases. Our research introduces a novel factor in PSC-IBD pathogenesis, that is, OMVs. These vesicles are released by pathobionts residing in the gut and can translocate from the intestinal lumen to the liver; there they exhibit a remarkable capacity to modulate the host immune system. In line with our study, a previous preclinical work by the Stappenbeck laboratory delved into the mechanisms through which intestinal symbiotic organisms interact with the host immune system, with a particular focus on the mechanisms enabling microbes or their antigens to access specific host immune cells.[8] Using genetically susceptible mice prone to develop spontaneous colitis in response to *Bacteroides thetaiotaomicron*, they uncovered that antigens derived from this bacterium gain access to the host by using OMVs.[8] Here, we identified that OMVs originating from gut pathobionts are associated with a heightened bacterial sensing in the liver. These OMVs trigger an augmented increase of the NLRP3 inflammasome, consequently promoting liver inflammation and fibrosis through mechanisms that involve TLR-dependent and -independent pathways. This discovery underscores the potential role of gut-derived OMVs in initiating and perpetuating not only intestinal, but also liver inflammation and fibrosis. In line with our work, previous animal studies have demonstrated the presence of serum LPS in the context of liver fibrosis, yet they were unable to demonstrate translocation of intact bacteria in a clinical setting.[2] Although intact bacteria showed only a limited ability to breach the mucosal barrier, our current observations strongly indicate the remarkable capability of OMVs to

overcome the gut–liver axis. We have visualized OMVs at the basolateral and luminal sides of the biliary epithelium, as well as at the luminal surface of endothelial cells of the portal vein. This suggests the potential of OMVs to access the liver through 2 distinct routes. The hypothesis of translocation via the bloodstream is substantiated by the presence of LPS-positive extracellular vesicles in the serum of individuals with PSC-IBD. Studies conducted by the Schramm laboratory have unveiled the presence of biliary dysbiosis, characterized by reduced biodiversity and an increase in pathogenic bacteria. Notably, our observations of OmpC-positive signals on the luminal surface of biliary epithelial cells, as well as the uptake of OMVs by ductal cells, support the notion that transmission through the biliary system may hold significant relevance in this context.[21] This concept gains further support from a substantial body of evidence pointing toward the involvement of disrupted bile duct epithelial tight junctions in the pathogenesis of PSC.[22,23] These disruptions could potentially facilitate translocation of OMVs from the luminal side across the ductal barrier. Nevertheless, further studies are necessary to elucidate the precise mechanisms through which bacterial vesicles, either directly or indirectly, influence the function of the ductal barrier in patients with PSC and via which transmission route they enter the liver.

Regardless of the specific transmission route, our research findings suggest that the presence of intestinal inflammation and/or microbial dysbiosis may contribute to the translocation of OMVs from the intestinal lumen to the liver. This conclusion is based on the absence of OmpC-positive signals in the livers of *Mdr2*-deficient animals and in patients with PSC who do not exhibit clinically manifest IBD. We noted significant occurrences of regulated necrosis in the intestinal epithelium, which could potentially serve as a significant pathogenic feature shared between PSC-IBD and the preclinical mouse model; that comes along with microbial dysbiosis and mucosal inflammation, irrespective of barrier dysfunction.[14–17] In line with these data, our findings suggest that OMVs play a role in the pro-inflammatory and pro-fibrogenic effects observed in the gastrointestinal tract. This conclusion is further supported by our in vivo experiments, when we administered OMVs to *Mdr2*$^{-/-}$ mice, leading to the initiation of inflammation and the acceleration of fibrosis in the context of genetic predisposition. These findings collectively illustrate that once OMVs have traversed the mucosal barrier, pathogenic mechanisms within the liver can be activated locally, without necessitating additional signals from the gut. Importantly, although OMVs may contribute to these effects, additional factors likely also play a role in shaping the dynamics of the gut–liver axis. Further research is needed to fully elucidate the multifaceted interactions involved. A recent study discovered that distinct luminal bacterial subsets in *Mdr2*$^{-/-}$ mice can either worsen or alleviate liver inflammation and fibrosis, with vancomycin-sensitive populations having an antifibrotic effect by modulating bile acid homeostasis and short-chain fatty acids.[13] *Lachnospiraceae*, in particular, reduced hepatic inflammation and fibrosis by increasing short-chain fatty acid levels and enhancing intestinal barrier function, and reduced *Lachnospiraceae* levels were observed in patients with PSC, potentially linking their reduction to increased OMV translocation, although further research is needed to confirm these correlations in systemic circulation and the liver. A recent study found that intestinal barrier dysfunction and bacterial translocation, triggered by LPS may protect against cholestatic liver diseases by affecting hepatic inflammation and bile acid metabolism through the NF-κB pathway, potentially mitigating disease progression.[24] Differences in these experimental data may be attributed to environmental factors, the experimental setup, as well as our limited knowledge regarding the cargo of OMVs. Both studies illustrate the complex inter-organ communication and emphasize further research addressing fine-tuned microbiota–host interactions.

In conclusion, our study contributes significant insights into the complex interplay among the gut pathobionts, bacterial OMVs, and liver-resident cell populations in the context of PSC-IBD. These findings expand our understanding of the multifactorial etiology of PSC-IBD and offer promising avenues for both diagnostic and therapeutic advancements in the field. Further research is needed to explore the precise origin and transmission routes of these OMVs and to develop targeted interventions for patients with PSC-IBD.

Supplementary Material

Note: To access the supplementary material accompanying this article, visit the online version of *Gastroenterology* at www.gastrojournal.org, and at https://doi.org/10.1053/j.gastro.2024.06.032.

References

1. **Hov JR, Karlsen TH**. The microbiota and the gut-liver axis in primary sclerosing cholangitis. Nat Rev Gastroenterol Hepatol 2023;20:135–154.
2. Nakamoto N, Sasaki N, Aoki R, et al. Gut pathobionts underlie intestinal barrier dysfunction and liver T helper 17 cell immune response in primary sclerosing cholangitis. Nat Microbiol 2019;4:492–503.
3. Liu Q, Li B, Li Y, et al. Altered faecal microbiome and metabolome in IgG4-related sclerosing cholangitis and primary sclerosing cholangitis. Gut 2022;71:899–909.
4. Vieira-Silva S, Sabino J, Valles-Colomer M, et al. Quantitative microbiome profiling disentangles inflammation- and bile duct obstruction-associated microbiota alterations across PSC/IBD diagnoses. Nat Microbiol 2019;4:1826–1831.
5. **Sabino J, Vieira-Silva S**, Machiels K, et al. Primary sclerosing cholangitis is characterised by intestinal dysbiosis independent from IBD. Gut 2016;65:1681–1689.
6. Toyofuku M, Schild S, Kaparakis-Liaskos M, et al. Composition and functions of bacterial membrane vesicles. Nat Rev Microbiol 2023;21:415–430.
7. **Bittel M, Reichert P**, Sarfati I, et al. Visualizing transfer of microbial biomolecules by outer membrane vesicles in microbe-host-communication in vivo. J Extracell Vesicles 2021;10:e12159.

8. **Hickey CA, Kuhn KA**, Donermeyer DL, et al. Colitogenic *Bacteroides thetaiotaomicron* antigens access host immune cells in a sulfatase-dependent manner via outer membrane vesicles. Cell Host Microbe 2015; 17:672–680.
9. **Kaparakis-Liaskos M, Ferrero RL**. Immune modulation by bacterial outer membrane vesicles. Nat Rev Immunol 2015;15:375–387.
10. Tulkens J, Vergauwen G, Van Deun J, et al. Increased levels of systemic LPS-positive bacterial extracellular vesicles in patients with intestinal barrier dysfunction. Gut 2020;69:191–193.
11. **Liao L, Schneider KM**, Galvez EJC, et al. Intestinal dysbiosis augments liver disease progression via NLRP3 in a murine model of primary sclerosing cholangitis. Gut 2019;68:1477–1492.
12. Ikenaga N, Liu SB, Sverdlov DY, et al. A new *Mdr2*$^{-/-}$ mouse model of sclerosing cholangitis with rapid fibrosis progression, early-onset portal hypertension, and liver cancer. Am J Pathol 2015;185:325–334.
13. Awoniyi M, Wang J, Ngo B, et al. Protective and aggressive bacterial subsets and metabolites modify hepatobiliary inflammation and fibrosis in a murine model of PSC. Gut 2023;72:671–685.
14. Gunther C, Buchen B, He GW, et al. Caspase-8 controls the gut response to microbial challenges by Tnf-alpha-dependent and independent pathways. Gut 2015; 64:601–610.
15. Gunther C, Martini E, Wittkopf N, et al. Caspase-8 regulates TNF-alpha-induced epithelial necroptosis and terminal ileitis. Nature 2011;477:335–339.
16. Gunther C, Ruder B, Stolzer I, et al. Interferon lambda promotes paneth cell death via STAT1 signaling in mice and is increased in inflamed ileal tissues of patients with Crohn's disease. Gastroenterology 2019; 157:1310–1322.e13.
17. Stolzer I, Kaden-Volynets V, Ruder B, et al. Environmental microbial factors determine the pattern of inflammatory lesions in a murine model of Crohn's disease-like inflammation. Inflamm Bowel Dis 2020;26:66–79.
18. Wang X, Eagen WJ, Lee JC. Orchestration of human macrophage NLRP3 inflammasome activation by *Staphylococcus aureus* extracellular vesicles. Proc Natl Acad Sci U S A 2020;117:3174–3184.
19. Gomes MTR, Cerqueira DM, Guimaraes ES, et al. Guanylate-binding proteins at the crossroad of noncanonical inflammasome activation during bacterial infections. J Leukoc Biol 2019;106:553–562.
20. Schnabl B, Choi YH, Olsen JC, et al. Immortal activated human hepatic stellate cells generated by ectopic telomerase expression. Lab Invest 2002;82:323–333.
21. **Liwinski T, Zenouzi R**, John C, et al. Alterations of the bile microbiome in primary sclerosing cholangitis. Gut 2020;69:665–672.
22. Rao RK, Samak G. Bile duct epithelial tight junctions and barrier function. Tissue Barriers 2013;1:e25718.
23. Xu J, Kausalya PJ, Van Hul N, et al. Protective functions of ZO-2/Tjp2 expressed in hepatocytes and cholangiocytes against liver injury and cholestasis. Gastroenterology 2021;160:2103–2118.
24. Gui W, Hole MJ, Molinaro A, et al. Colitis ameliorates cholestatic liver disease via suppression of bile acid synthesis. Nat Commun 2023;14:3304.

Author names in bold designate shared co-first authorship.

Received October 20, 2023. Accepted June 24, 2024.

Correspondence
Address correspondence to: Claudia Günther, PhD, Department of Medicine 1, Universitätsklinikum Erlangen, Kussmaulallee 4, 91054 Erlangen, Germany. e-mail: c.guenther@uk-erlangen.de.

Acknowledgments
The authors thank Daniel Beß, Jennifer Redlingshöfer, Elena Percivalle, Chaofan Liu, and Ilann Sarfati for excellent technical assistance. The Graphical Abstract, Figure 1*A*, Figure 3*A*, and Supplementary Figure 3*A* were created with BioRender.com.

CrediT Authorship Contributions
Heidrun Dorner (Conceptualization: Supporting; Formal analysis: Equal; Investigation: Equal; Visualization: Equal; Writing – original draft: Equal; Writing – review & editing: Equal)
Iris Stolzer, PhD (Conceptualization: Supporting; Formal analysis: Equal; Investigation: Equal; Visualization: Equal; Writing – original draft: Equal; Writing – review & editing: Equal)
Jochen Mattner, MD (Resources: Equal; Writing – review & editing: Equal)
Sophie Kaminski (Investigation: Supporting; Writing – review & editing: Equal)
Sofia Leistl, MSc (Investigation: Supporting; Writing – review & editing: Equal)
Lisa-Maria Edrich (Investigation: Supporting; Writing – review & editing: Equal)
Raphael Schwendner (Investigation: Supporting; Writing – review & editing: Equal)
Julia Hobauer (Investigation: Supporting; Writing – review & editing: Equal)
Adrian Sebald (Investigation: Supporting; Writing – review & editing: Equal)
Stefanie Leikam (Investigation: Supporting; Writing – review & editing: Equal)
Miguel Gonzalez Acera, MSc (Formal analysis: Lead; Writing – review & editing: Equal)
Miriam Düll, MD (Resources: Equal; Writing – review & editing: Equal)
Roland Lang, MD (Resources: Equal; Writing – review & editing: Equal)
Gerald Seidel, PhD (Resources: Equal; Writing – review & editing: Equal)
Tatjana Seitz, PhD (Resources: Equal; Writing – review & editing: Equal)
Claus Hellerbrand, MD (Resources: Equal; Writing – review & editing: Equal)
Gregor Fuhrmann, PhD (Resources: Equal; Writing – review & editing: Equal)
Ute Distler, PhD (Investigation: Supporting; Writing – review & editing: Equal)
Stefan Tenzer, PhD (Resources: Equal; Writing – review & editing: Equal)
Phillip Eichhorn, MD (Resources: Equal; Writing – review & editing: Equal)
Michael Vieth, MD (Resources: Equal; Writing – review & editing: Equal)
Christoph Schramm, MD (Resources: Equal; Writing – review & editing: Equal)
Philipp Arnold, PhD (Investigation: Supporting; Writing – review & editing: Equal)
Christoph Becker, PhD (Resources: Equal; Writing – review & editing: Equal)
Carl Weidinger, MD (Resources: Equal; Writing – review & editing: Equal)
Britta Siegmund, MD (Resources: Equal; Writing – review & editing: Equal)
Raja Atreya, MD (Resources: Equal; Writing – review & editing: Equal)
Moritz Leppkes, MD (Resources: Equal; Writing – review & editing: Equal)
Elisabeth Naschberger, PhD (Resources: Equal; Writing – review & editing: Equal)
Fotios Sampaziotis, MD, PhD (Resources: Equal; Writing – review & editing: Equal)
Peter Dietrich, MD (Resources: Equal; Writing – review & editing: Equal)
Manfred Rauh, PhD (Investigation: Supporting; Writing – review & editing: Equal)
Stefan Wirtz, PhD (Investigation: Supporting; Writing – review & editing: Equal)
Andreas E. Kremer, MD (Conceptualization: Equal; Resources: Equal; Writing – review & editing: Equal)
Markus F. Neurath, MD (Conceptualization: Lead; Resources: Equal; Writing – review & editing: Equal)
Claudia Günther, PhD (Conceptualization: Lead; Formal analysis: Equal; Resources: Lead; Visualization: Equal; Writing – original draft: Equal; Writing – review & editing: Equal)

Conflicts of interest
The authors disclose no conflicts.

Funding
This research has received funding from the Deutsche Forschungsgemeinschaft (DFG [German Research Foundation]) TRR 241–375876048 (A02; A03; A09; B01; B04; C02; C03; C04; Z03), FOR 2886–405969122 (A02), TRR305–429280966 (B08; B11; B12), KFO5024–505539112 (A01; A03; A04; B01; B03; B04; Z01), TRR369- 501752319 (A02), and DFG GU 1431/5-1, DFG DFG-MA 2621/5-1 and DFG KR 3618/5-1. Further support was provided by the Interdisciplinary Center for Clinical Research of the Friedrich-Alexander-Universität Erlangen-Nürnberg (Jochen-Kalden funding program N5, ELAN P119).

Supplementary Materials and Methods

Human Samples

All studies with human material were approved by the Ethics Committee (#49_16B) of the Universitätsklinikum Erlangen. Human tissue samples were obtained from patients undergoing routine biopsy collection at the Universitätsklinikum Erlangen, after written informed consent was obtained from the patients. Liver tissues were used for either paraffin-embedded sections or frozen cryosections. The diagnoses of PSC and PSC-IBD were based on clinical, endoscopic, radiology, and histologic findings. Data were pseudonymized. A comprehensive description of the patient cohorts is presented in Supplementary Table 1.

Animals and Housing

Rosa26.tdTomato,[7] *Casp8*$^{\Delta IEC}$,[15] *Mdr2*$^{-/-}$,[e1] *Myd88*$^{-/-}$,[e2] and *Gsdmd*$^{-/-}$[e3] mice were described previously. *Casp8*$^{\Delta IEC}$x*Mdr2*$^{-/-}$ were generated by crossing *Casp8*$^{\Delta IEC}$ mice to *Mdr2*$^{-/-}$ mice. Mice were housed under specific-pathogen–free conditions and were routinely screened for pathogens according to Federation of European Laboratory Animal Science Associations guidelines. DNA was extracted from ear tissue biopsy and genotyping was performed by polymerase chain reaction, as described for the individual strains. Control (*Casp8*^{fl}x*Mdr2*$^{+/-}$), *Mdr2*$^{-/-}$ and *Casp8*$^{\Delta IEC}$x*Mdr2*$^{-/-}$ mice were sacrificed at 30–35 weeks and experiments were repeated n $\leq$ 2 times with similar results. Animal studies were conducted in a sex- and age-matched manner and littermates were used to exclude strain-dependent differences in susceptibility for each experiment. Animal experiments were performed in accordance with the Federation of European Laboratory Animal Science Associations welfare regulations. Animal protocols were approved by the Animal Care and Use Committee.

In Vivo Model to Visualize the Transfer of Bacterial-Derived Extracellular Vesicles

Treatment of *Rosa26.tdTomato* mice were described previously.[7] In brief, *Rosa26.tdTomato* mice were pretreated with a broad-spectrum oral antibiotic cocktail via drinking water for 6 days (days 1–6) to reduce the endogenous microbiota. To generate a selective ecological niche for the used *E coli* strains, antibiotic treatment was switched to selection antibiotic treatment with ampicillin (1 g/L) via drinking water on day 7 to prevail against the endogenous microbiota. On days 8–11, mice were inoculated daily via oral gavage with either ampicillin-resistant *E coli*^{Cre} (3×10^9 *E coli*^{Cre} [plus 3×10^9 *E coli*^{GFP} intial dose, day 8]) or *E coli*^{GFP} (6×10^9 *E coli*^{GFP}]) as control. Bacterial abundance (colony-forming unit/g stool) was verified from fecal samples on days 0, 6, and 12 on Luria broth-Agar plates without and with ampicillin (100 mg/L). In order to enhance gut barrier permeability facilitating bacterial vesicle transmigration, mice were injected twice intraperitoneally with 2.5 mg lipopolysaccharide/kg body weight (days 10 and 11). On day 12, mice were sacrificed and organs were harvested.

Outer Membrane Vesicle Treatment of Mdr2$^{-/-}$ Mice

Mdr2$^{-/-}$ mice (aged approximately 15 weeks) were injected intraperitoneallywith phosphate-buffered saline (PBS) (mock) or OMVs derived from pathogenic bacteria as follows: on day 1: *K pneumonia* (1×10^9 particles in 100 μL PBS); on day 2: *P mirabilis* (2×10^9 particles in 100 μL PBS); and on day 8: *P mirabilis* (1×10^9 particles in 100 μL PBS). Assessment of health status and evaluation of body weight were performed daily until day 9 and every second day until day 15. Mice were sacrificed and analyzed on day 15.

Tissue Collection

Tissue for histology and immunohistochemistry were collected and fixed in 4.5% formaldehyde. Tissue was embedded in paraffin in a water-free procedure and stored at room temperature for further analysis. Samples for cryosections and RNA analyses were instantly frozen in liquid nitrogen and stored at −80°C until further use.

Gene Expression

Total RNA was extracted by using the NucleoSpin RNA Mini-kit for RNA purification (Macherey-Nagel). Complementary DNA was synthesized using the SCRIPT cDNA Synthesis Kit (Jena Bioscience). Real-time polymerase chain reaction analysis was performed using LightCycler 480 SYBR Green I Master (Roche) and gene-specific primers (Supplementary Table 2) were used. Experimental values were normalized to levels of the indicated housekeeping gene and for fold-change calculation, the mean of the relative expression of controls was set as 1.

Histology and Immunohistochemistry

Histopathologic analyses were performed on formalin-fixed, paraffin-embedded tissue after Mayer's hematoxylin and eosin staining and Sirius Red staining. For immunohistochemical analysis, frozen tissue slices were fixed on glass slides using 4% paraformaldehyde, and paraffin-embedded tissue sections were dewaxed and rehydrated. Immunofluorescence staining of tissue sections was performed using directly labeled secondary antibody or biotin-streptavidin system via DyLight or TSA System, as recommended by the manufacturer. Used antibodies and the labeling system are listed in Supplementary Table 3. Nuclei were counterstained with Hoechst 33342. Staining of GBP1 was performed as described previously.[e4] Cell death was analyzed via terminal deoxynucleotidyl transferase–mediated deoxyuridine triphosphate nick-end labeling using the in situ cell death detection kit (Roche). Detection of bacteria in tissue sections was performed by fluorescence in situ hybridization using a universal bacterial oligonucleotide probe, EUB-338 (5′-GCT GCC TCC CGT AGG AGT-3′). The tissue was incubated with the probe, dissolved in formamide containing hybridization buffer at 46°C, as described previously.[e5] Images were obtained using a confocal fluorescence microscope LEICA TCS SP5 II, the LEICA DMI 4000B microscope together with the LEICA DFC360 FX or LEICA DFC420 C camera or the Leica DMi1 microscope with the corresponding imaging software

or with a slide scanner system from Hamamatsu and the corresponding NDPView2 software.

Quantification of Sirius Red Staining and Immunohistochemistry

Sirius Red–stained slides were scanned with the slide scanner system from Hamamatsu. Pictures were processed and analyzed with QuPath[e6] and the Liver Quant script.[e7] Annotations were performed manually and for each slide 3–6 regions of interest (ROIs) were set randomly. Immunohistochemistry-stained slides were recorded using a LEICA TCS SP5 II confocal fluorescence microscope and pictures were analyzed with ImageJ software.[e8] The thresholds of individual channels were adjusted and either the positive area was measured or the amount of particles was calculated with the particle analyzer tool.

RNA Sequencing

Total RNA was sent to Novogene for bulk animal eukaryotic mRNA sequencing with the Illumina Sequencing PE150 sequencing platform and strategy and library type mRNA library preparation (poly A enrichment). The obtained paired-end reads were mapped against the mouse reference genomes and annotation was obtained from Ensembl (GRCm39) using STAR software (version 2.7.0d).[e9] Counts for the samples were obtained using FeatureCounts (version 2.0.1).[e10] Differential expression between the sample groups was performed using the DESeq2 (version 1.40.2) package in R.[e11] Further analysis of the samples and graphic displays was performed using in-house software.

Bacterial Strains

E coli^{Cre} and *E coli*^{GFP} were described previously.[7] *E coli* BL21 (DE3) (Thermo Scientific) containing an ampicillin-resistance gene and ClearColi BL21 (DE3) (Biosearch Technologies, kanamycin resistance) containing a kanamycin-resistance gene. *K pneumonia* and *P mirabilis* were patient-derived isolates (urin) and provided by the Microbiology Institute-Clinical Microbiology, Immunology and Hygiene of the Universitätsklinikum Erlangen. The classification as pathobionts was based on the detection of various pathogenic factors, which could be molecularly demonstrated. Detailed characterization of *Klebsiella* strains is presented in Supplementary Figure 9.

Bacterial Culture

Bacterial strains were cultured at 37°C in Luria broth media supplemented with selection antibiotic, if required, under continuous shaking and aeration. Bacterial culture was incubated until exponential growth phase was reached, centrifuged (1 hour, 5000 × g, 4°C) and the supernatant was collected. The collected supernatant was filtered (0.22 μm) and further processed.

Isolation of Outer Membrane Vesicles

Bacterial strains were cultured and processed as described above. OMVs were isolated via either polyethylene glycol precipitation or ultracentrifugation.

For vesicle precipitation with polyethylene glycol, the filtrated bacterial supernatant was mixed with polyethylene glycol 8000 (1:5) and incubated at 4°C overnight. After incubation, the samples were centrifuged (30 minutes, 7100 × g, 4°C), the supernatant was discarded, and the pellets were pooled with a small amount of residual supernatant. The samples were transferred into ultrafiltration tubes and centrifuged (10 minutes, 2500 × g, 4°C). The supernatant was discarded except for a small residual and the pellets were resuspended and pooled into one 2-mL tube. The samples were centrifuged (20 minutes, 18,000 × g, 4°C), the supernatant was discarded, and the received pellet was resuspended in sterile particle-free PBS.

For vesicle precipitation with ultracentrifugation, the filtrated bacterial supernatant was divided into ultracentrifugation tubes and centrifuged (2 hours, 110,000 × g, 4°C). After discarding the supernatant, the pellets were resuspended and pooled in sterile PBS. The sample was divided into ultracentrifugation reaction tubes and centrifuged again (2 hours, 110,000 × g, 4°C). The pellets were resuspended and pooled in sterile particle-free PBS. Isolated bacterial vesicles were stored at 4°C and further analyzed concerning concentration and purity bevor use. Detailed characterization of used OMVs is presented in Supplementary Figure 9.

Bacterial Genome Sequencing

High-molecular-weight genomic DNA of *K pneumoniae* strains was extracted from pelleted overnight cultures using Genomic-tips 20 columns (Qiagen, Hilden, Germany) and fluorometrically quantified using a Qubit device (ThermoFisher). Sequencing libraries were prepared using Ligation Sequencing Kit V14 (SQK-LSK114, Oxford Nanopore) and sequenced using R10.4.1 flow cells (Oxford Nanopore) on a Minion Mk1B device. Dorado, version 0.5 in super-accuracy mode was used for base-calling and fastq file generation. De novo genomic assembly was conducted using Flye, version 2.9.3[e12] in "nano-hq" mode, followed by 3 rounds of polishing. Bandage, version 0.9e13 was used for visual inspection of the assemblies of final genomes and plasmids and checkm2[e14] was used to predict the completeness and contamination of the assemblies.

Annotation of genomic and plasmid contigs was performed using Bakta, version 1.8.2.[e15] AMRfinder, version 3.12.8[e16] and Kleborate, version 2.4.0[e17] were used for serotype and virulence factor prediction.

Liquid Chromatography Mass Spectrometry Analysis

Proteins derived from isolated bacterial membrane vesicles were extracted using a sodium dodecyl sulfate–based buffer at a final concentration of 1.6% (w/v) sodium dodecyl sulfate and digested using single-pot solid-phase-enhanced sample preparation (SP3), as detailed previously.[e18,e19] In brief, samples were first reduced and alkylated using dithiothreitol and iodoacetamide, respectively. Excess iodoacetamide was quenched by the addition of dithiothreitol. Afterwards, 2 μL of carboxylate-modified

paramagnetic beads (Sera-Mag SpeedBeads, GE Healthcare), 0.5 μg solids/μL in water, as described by Hughes et al,[e19] were added to the samples. After adding acetonitrile to a final concentration of 70% (v/v), samples were allowed to settle at room temperature for 20 minutes. Subsequently, beads were washed twice with 70% (v/v) ethanol in water and once with acetonitrile. Afterwards, beads were resuspended in 50 mM NH_4HCO_3 supplemented with trypsin (Mass Spectrometry Grade; Promega) and incubated overnight at 37°C. After overnight digestion, acetonitrile was added to the samples to reach a final concentration of 95% (v/v). After 20 minutes of incubation at room temperature, beads were washed with acetonitrile. To recover bound peptides, paramagnetic beads were sonicated in 2% (v/v) dimethyl sulfoxide in water for 1 minute. After 5 minutes of centrifugation at 13,000 rpm (4°C), supernatants containing tryptic peptides were collected and acidified with 0.1% (v/v) formic acid for mass spectrometry (MS) analysis. Subsequently, tryptic peptides were analyzed on an Evosep One (Evosep, Odense, Denmark) liquid chromatography system equipped with a PepSep C18 1.5 μm, 150 μm $\times$ 80 mm analytical reversed-phase column (Bruker Corporation). The Evotips for each run were loaded with 20 μL peptide solution containing approximately 250 ng of sample peptides. They were placed in the Evosep One autosampler until analysis. The 60 samples per day method using a 24-minute gradient was chosen. Mobile phase A was water containing 0.1% (v/v) formic acid and mobile phase B was acetonitrile containing 0.1% (v/v) formic acid. Column temperature was set to 40°C. MS analysis of eluting peptides was conducted on a timsTOF HT instrument platform (Bruker Corporation) equipped with a CaptiveSpray ion source. The MS was operated in data-dependent acquisition parallel accumulation-serial fragmentation mode. Ion accumulation and separation using trapped ion mobility spectrometry was set to a ramp time of 100 ms with an ion mobility range ($1/K_0$) from 0.6 to 1.6 Vs/cm^2. One MS cycle included 1 trapped ion mobility spectrometry full MS scan and 10 parallel accumulation–serial fragmentation scans with up to 12 precursors targeted per scan. Data were acquired in positive mode and samples were analyzed in triplicate. MS data were processed and analyzed using PEAKS Studio (version 10.6, Bioinformatics Solutions). Data were searched against a custom-compiled *E coli* Bl21 (UP000475070), *E coli* Nissle (UP000001410), *K pneumoniae* (UP000007841), and *Proteus myxofaciens* (UP000094023) proteome databases (UniProtKB Swiss-Prot/TrEMBL release April 2024), all containing a list of common contaminants. For database search, the following parameters were applied: 1) trypsin as enzyme for digestion, 2) up to 2 missed cleavages per peptide, 3) carbamidomethyl cysteine as fixed, and 4) methionine oxidation, as well as acetylation (N-term), as variable modifications. The false discovery rate for peptide and protein identification was assessed using the target-decoy strategy by searching a reverse database and was set to 0.01 on both the protein and peptide level. Proteins had to be identified by at least 2 peptides.

Serum-Derived Vesicles

After collection of the whole blood by phlebotomy, blood was allowed to clot by leaving it undisturbed at room temperature for 15–30 minutes. Clotted blood was centrifuged for 10 minutes at 1300 $\times$ g. Serum was collected and frozen until further use at –80°C. Vesicles were isolated with the Total Exosome Isolation (from serum) Kit (Invitrogen), according to the user manual. Serum samples were thawed and centrifuged for 30 minutes at 200 $\times$ g and 4°C. Serum was transferred into a new reaction tube; 0.2 volumes of the total exosome isolation reagent was added and the sample was vortexed and incubated for 30 minutes at 4°C. Samples were centrifuged at 10,000 $\times$ g for 10 minutes and supernatant was discarded. The pallet was resuspended with particle-free PBS and isolated vesicles were stored at 4°C and further analyzed concerning concentration and purity bevor use.

Analyses of Concentration and Purity of Isolated Bacterial and Serum-Derived Vesicles

To determine the concentration of vesicles in each sample, nanoparticle tracking analysis using the ZetaView (Particle Metrix) was performed with a detection wavelength at 488 nm using ZetaView software. Samples were diluted suitably. Transmission electron microscopy of extracellular vesicle samples was, in principle, performed as described previously,[e20] with the exception that 3 μL of sample was added to a freshly discharged continuous carbon grid (Science Service, Munich, Germany). Images were acquired at a nominal magnification of 30 kX on a JEOL 1400Plus transmission electron microscopy (JEOAL) operating at an acceleration voltage of 120 kV.

Lipopolysaccharide Detection/Toll-Like Receptor 4 Reporter Assay

The TLR4 reporter assay was performed with the HEK-Blue Lipopolysaccharide Detection Kit 2 from InvivoGen. In summary, Hek-Blue 4 cells were cultured in Dulbecco's modified Eagle medium (DMEM) supplemented with GlutaMax (1$\times$), penicillin-streptomycin (1%), 10% value fetal bovine serum, 1$\times$ Normocin, and 1$\times$ HEK-Blue Selection for up to 30 passages at 37°C and 5% CO_2. Routinely, the cells were splatted every 2 or 3 day (60%–80% confluency) with Trypsin-EDTA (0.05% Trypsin-EDTA diluted 1:3 in PBS). For the assay, cells were splatted with PBS only and seeded as 50,000 cells/well (96-well format) in medium without Normocin and without HEK-Blue Selection. Cells were treated with the standard as described in the user manual, equal amounts of human-derived extracellular vesicles or bacterial-derived vesicles. Cells were incubated for 18–24 hours at 37°C and 5% CO_2. After incubation, 20 μL supernatant were transferred into a new 96-well plate and prewarmed QUANTI-Blue solution was added. Plate was incubated at 37°C and plate was measured after 4 hours at 420 nm.

Cell and Organoid Culture

Human hepatic stellate cell line HSZ-B were cultured in DMEM supplemented with GlutaMAX (1×), penicillin-streptomycin (1%), and 10% fetal calf serum at 37°C and 5% CO_2. Murine J774A.1 cells were cultured in DMEM supplemented with penicillin-streptomycin (1%) and 10% fetal calf serum at 37°C and 5% CO_2.

Bile duct organoids were isolated from the intra- or extrahepatic bile ducts and plated in a basement membrane matrix and cultured in specific organoid medium. For detailed information, see below.

In Vitro Stimulation and Analysis

Organoids and cells were treated with indicated amounts of particles per milliliter of OMVs per strain in corresponding medium or mock (PBS) treated. Organoids and cells were treated with 8.6–10 × 10^8 particles/mL (exception: experiment Figure 2*J* and *K*: 8 × 10^9 particles/mL). Organoids were stained with propidium iodide staining solution (BD Pharmingen). Time-lapse microscopy was performed using the EVOS M7000 Imaging System (Invitrogen). Cytotoxic reaction of organoids treated with OMVs was quantified via lactate dehydrogenase assay in the culture supernatant using the Cytotoxicity Detection Kit (Roche) according to the manufacturer's protocol. Viability of HSZ-B cells were analyzed using the Incucyte SX5 (Sartorius) system.

Murine Intrahepatic Bile Duct Organoid Culture System

Intraheptic bile duct organoids were isolated from liver tissue and cultured for a minimum of 14 days, as described by Broutier et al.[e21] In brief, intrahepatic bile ducts were isolated by incubating the minced liver without the gallbladder and extrahepatic bile ducts in a digestion solution containing 0.125 mg/mL collagenase IV and 0.125 mg/mL dispase II at 37°C for 1 hour. Supernatant of digested tissue was centrifuged (5 minutes, 300 × g, 4°C) and plated in a basement membrane matrix (Cultrex BME Type 2, R&D Systems or Matrigel, Corning) and cultured in murine liver isolation medium containing basal organoid medium (Advanced DMEM F12, Hepes (10 mM), GlutaMax (1×), 100 U/mL penicillin, 100 μg/mL streptomycin supplemented with R-spondin (20%), noggin (5%), B27 (1×), N-acetylcysteine (1 mM), nicotinamide (10 mM), gastrin (10 nM), epidermal growth factor (EGF) (50 ng/mL), hepatocyte growth factor (50 ng/mL), fibroblast growth factor-10 (100 ng/mL), forskolin (10 μM), Y-inhibitor (10 μM), and Wnt3a fusion protein (0.25 nM). After passaging the organoids once, the medium was changed to murine liver expansion medium (murine liver isolation medium without Wnt3a and Noggin).

Murine Extrahepatic Bile Duct Organoid Culture

Extrahepatic bile duct organoids were isolated from the gallbladder and extrahepatic bile as described by Huch et al.[e22] The murine gallbladder and extrahepatic bile ducts were harvested and the remaining liver tissue was removed. The gallbladder and bile ducts were minced and digested in 2.6 mM EDTA for 2 hours at 4°C. The supernatant was filtered (100 μM cell strainer) and centrifuged (5 minutes, 300 × g, 4°C). Isolated cells were plated in basement membrane matrix (Matrigel, Corning) and cultured in basal organoid medium supplemented with R-spondin (20%), noggin (5%), B27 (1×), N-acetylcysteine (625 μM), nicotinamide (10 mM), EGF (100 ng/mL), hepatocyte growth factor (50 ng/mL), fibroblast growth factor-10 (100 ng/mL), DAPT (40 μM), and Y-inhibitor (10 μM).

Human Extrahepatic Bile Duct Organoid Culture

Collected bile was centrifuged (5 minutes, 300 × g, 4°C). The pellet was plated in basement membrane matrix (Matrigel, Corning) and cultured in basal organoid medium supplemented with R-spondin (30%), noggin (10%), B27 (1×), N2 (1×), CHIR99021 (3 μM), prostaglandin E2 (2.5 μM), EGF (100 ng/mL), forskolin (10 μM), Y-inhibitor (10 μM), and A38-01 (5 μM).

Human Intrahepatic Bile Duct Organoid Culture

Liver biopsies were collected during minimally invasive laparoscopy and minced. The tissue pieces were digested in a digestion solution containing 0.125 mg/mL collagenase IV and 0.125 mg/mL dispase II at 37°C for 3 hours. After digestion, tissue fragments and the single cells in suspension were centrifuged (5 minutes, 300 × g, 4 C°) and plated in basement membrane matrix (Matrigel, Corning) and cultured in basal organoid medium supplemented with R-spondin (20%), noggin (10%), B27 (1×), N-acetylcysteine (1.25 mM), nicotinamide (10 mM), gastrin (10 nM), EGF (50 ng/mL), hepatocyte growth factor (25 ng/mL), fibroblast growth factor 10 (100 ng/mL), forskolin (10 μM), Y-inhibitor (10 μM), Wnt3a fusion protein (0.25 nM), N2 (1×), and A38-01 (5 μM).

Bile Acid Measurement

Individual bile acid species were measured by liquid chromatography MS. The deproteinized samples (25 μL) were injected into a API6500+ mass spectrometer using an Agilent system with autosampler (API6500+, Sciex Darmstadt, Germany, HPLC1260 series, Agilent Technologies, Waldbronn, Germany). Gradient chromatography was performed using an analytical column (Chromolith RP-18e) at 30°C. The mobile phases were methanol- and water-based (aqueous phase pH adjusted to 4.5) containing each 5 mM ammonium formate. Total flow rate for liquid chromatography was kept at 1 mL/min; total run time was 12 minutes. For scheduled multiple-reaction monitoring–based mass spectrometric detection electrospray ionization in negative mode was used. Deuterium-labeled unconjugated and glycine- and taurine-conjugated bile acids served as internal standards for quantification.

Statistical Analysis

All error bars indicate SD. Concerning statistical analysis, equal SD was assumed for in vitro experiments

and unequal SD was assumed for in vivo experiments. Comparisons of 2 groups were performed using a Welch's t test or unpaired t test. Comparisons among multiple groups were performed using ordinary 1-way analysis of variance with Tukey's multiple comparisons test, Brown-Forsythe and Welch analysis of variance with Dunnett's T3 multiple comparisons test, or 2-way analysis of variance with Šídák's multiple comparisons test. Statistical significance was accepted with $P < .05$ (NS [$P \geq .05$]; *$P < .05$; **$P < .01$; ***$P < .001$; ****$P < .0001$). All P values calculated using multiple comparison are given as multiplicity-adjusted P values. Statistical calculations were performed using GraphPad Prism, version 9.5.1.

Supplementary References

e1. Smit JJM, Schinkel AH, Oude Elferink RPJ, et al. Homozygous disruption of the murine *MDR2* P-glycoprotein gene leads to a complete absence of phospholipid from bile and to liver disease. Cell 1993;75:451–462.

e2. Adachi O, Kawai T, Takeda K, et al. Targeted disruption of the MyD88 gene results in loss of IL-1- and IL-18-mediated function. Immunity 1998;9:143–150.

e3. Kayagaki N, Stowe IB, Lee BL, et al. Caspase-11 cleaves gasdermin D for non-canonical inflammasome signalling. Nature 2015;526:666–671.

e4. Naschberger E, Liebl A, Schellerer VS, et al. Matricellular protein SPARCL1 regulates tumor microenvironment-dependent endothelial cell heterogeneity in colorectal carcinoma. J Clin Invest 2016;126:4187–4204.

e5. Becker C, Wirtz S, Blessing M, et al. Constitutive p40 promoter activation and IL-23 production in the terminal ileum mediated by dendritic cells. J Clin Invest 2003;112:693–706.

e6. Bankhead P, Loughrey MB, Fernandez JA, et al. QuPath: open source software for digital pathology image analysis. Sci Rep 2017;7:16878.

e7. Hellen DJ, Karpen SJ. LiverQuant: an improved method for quantitative analysis of liver pathology. Bio Protoc 2023;13:e4776.

e8. Schneider CA, Rasband WS, Eliceiri KW. NIH Image to ImageJ: 25 years of image analysis. Nat Methods 2012;9:671–675.

e9. Dobin A, Davis CA, Schlesinger F, et al. STAR: ultrafast universal RNA-seq aligner. Bioinformatics 2013;29:15–21.

e10. Liao Y, Smyth GK, Shi W. featureCounts: an efficient general purpose program for assigning sequence reads to genomic features. Bioinformatics 2014;30:923–930.

e11. Love MI, Huber W, Anders S. Moderated estimation of fold change and dispersion for RNA-seq data with DESeq2. Genome Biol 2014;15:550.

e12. Kolmogorov M, Yuan J, Lin Y, et al. Assembly of long, error-prone reads using repeat graphs. Nat Biotechnol 2019;37:540–546.

e13. Wick RR, Schultz MB, Zobel J, et al. Bandage: interactive visualization of de novo genome assemblies. Bioinformatics 2015;31:3350–3352.

e14. Chklovski A, Parks DH, Woodcroft BJ, et al. CheckM2: a rapid, scalable and accurate tool for assessing microbial genome quality using machine learning. Nat Methods 2023;20:1203–1212.

e15. Schwengers O, Jelonek L, Dieckmann MA, et al. Bakta: rapid and standardized annotation of bacterial genomes via alignment-free sequence identification. Microb Genome 2021;7:000685.

e16. Feldgarden M, Brover V, Gonzalez-Escalona N, et al. AMRFinderPlus and the Reference Gene Catalog facilitate examination of the genomic links among antimicrobial resistance, stress response, and virulence. Sci Rep 2021;11:12728.

e17. Lam MMC, Wick RR, Watts SC, et al. A genomic surveillance framework and genotyping tool for *Klebsiella pneumoniae* and its related species complex. Nat Commun 2021;12:4188.

e18. Hughes CS, Foehr S, Garfield DA, et al. Ultrasensitive proteome analysis using paramagnetic bead technology. Mol Syst Biol 2014;10:757.

e19. Sielaff M, Kuharev J, Bohn T, et al. Evaluation of FASP, SP3, and iST protocols for proteomic sample preparation in the low microgram range. J Proteome Res 2017;16:4060–4072.

e20. **Lipinski S, Pfeuffer S**, Arnold P, et al. Prdx4 limits caspase-1 activation and restricts inflammasome-mediated signaling by extracellular vesicles. EMBO J 2019;38:e101266.

e21. Broutier L, Andersson-Rolf A, Hindley CJ, et al. Culture and establishment of self-renewing human and mouse adult liver and pancreas 3D organoids and their genetic manipulation. Nat Protoc 2016;11:1724–1743.

e22. **Huch M, Dorrell C**, Boj SF, et al. In vitro expansion of single Lgr5+ liver stem cells induced by Wnt-driven regeneration. Nature 2013;494:247–250.

Author names in bold designate shared co-first authorship.

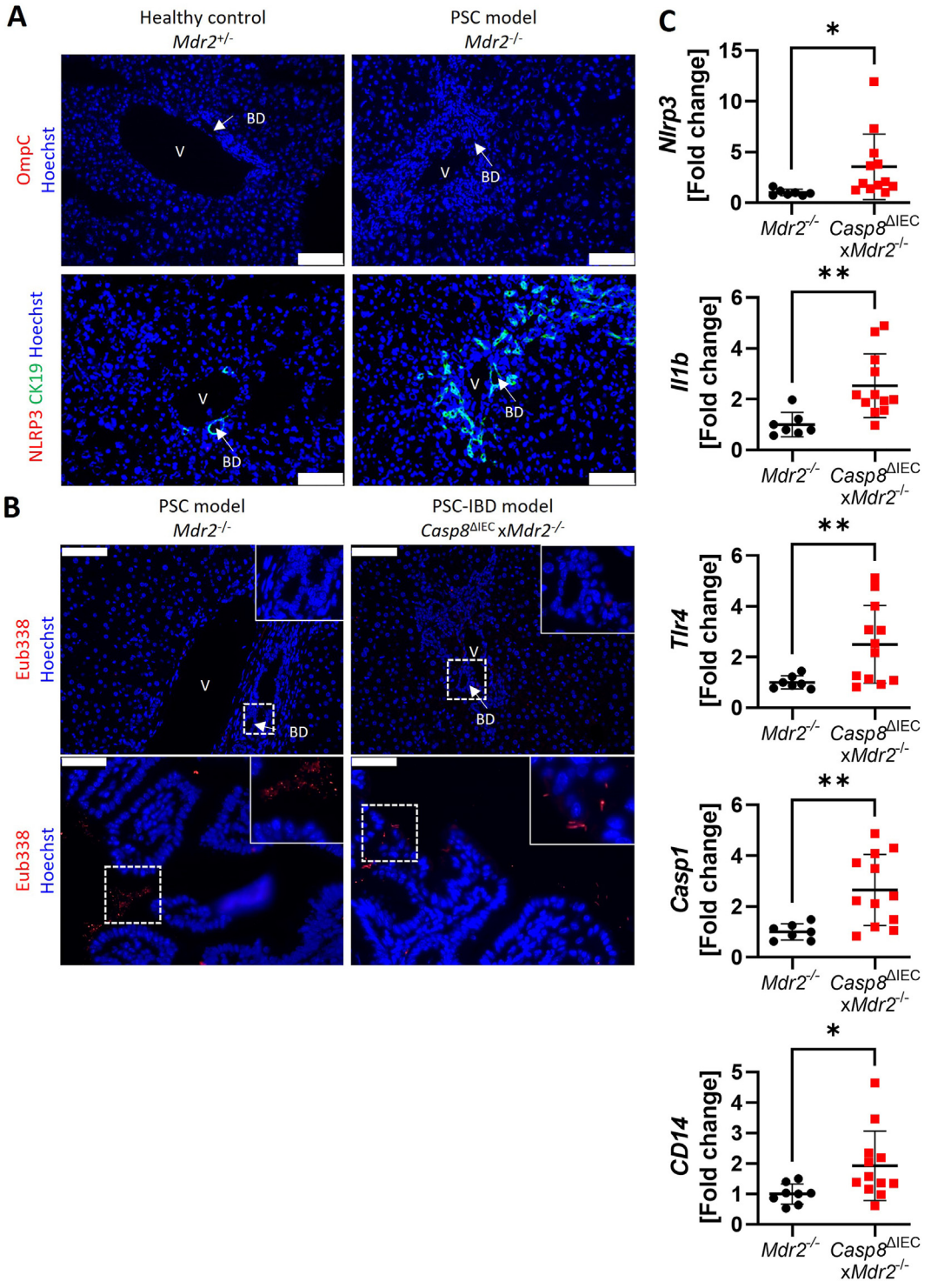

Supplementary Figure 1. Enhanced hepatic bacterial sensing in *Casp8*$^{\Delta IEC}$x*Mdr2*$^{-/-}$ mice. Mice were sacrificed at approximately 35 weeks. The experiment was repeated 3 times with similar results. (*A*) Representative *images* of liver cross sections immunohistochemically stained with antibodies against OmpC (*red*) or NLRP3 (*red*) and CK19 (*green*). *Scale bar:* 100 μm. BD, bile duct; V, vessel. (*B*) Representative *images* of fluorescence in situ hybridization staining using a universal eubacterial probe (Eub338, *red*) in liver (*upper*, *scale bar:* 100 μm) and intestinal (*lower*, *scale bar:* 50 μm) cross sections. (*C*) Gene transcription analysis of hepatic mRNA expression normalized to *Hprt*. Pooled data of independent experiments. *Mdr2*$^{-/-}$ n = 7, *Casp8*$^{\Delta IEC}$x*Mdr2*$^{-/-}$ n = 12, statistical test: Welch's *t* test. **P* < .05; ***P* < .01.

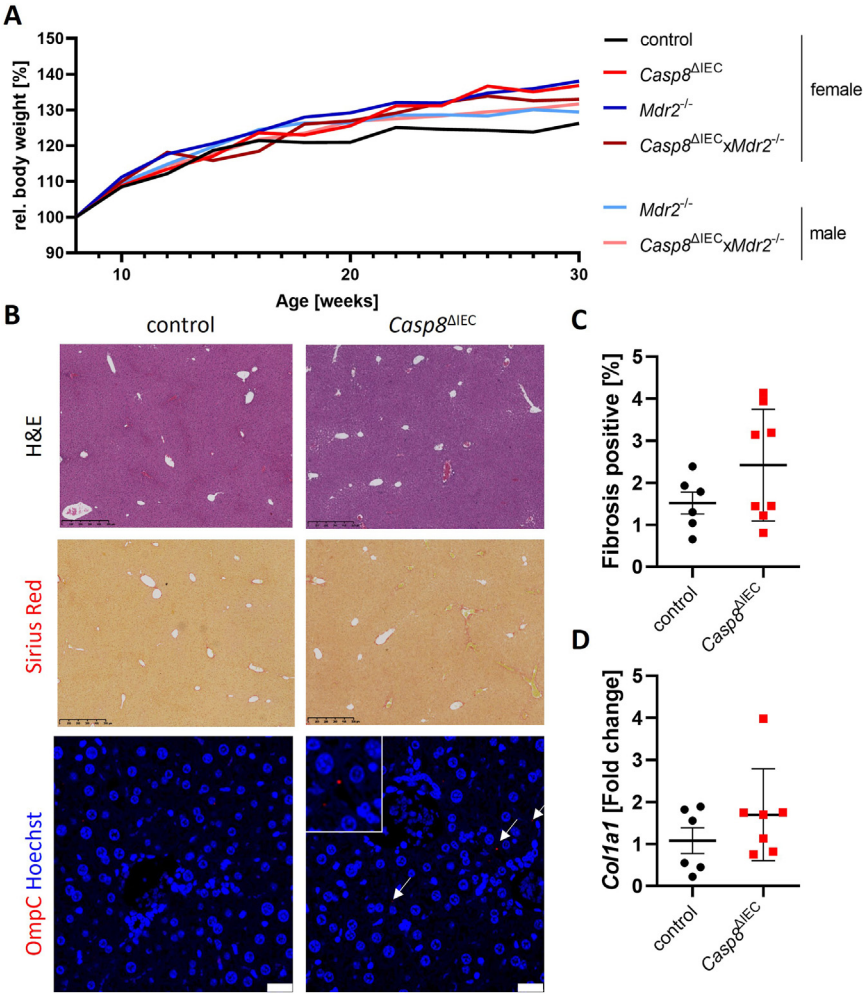

Supplementary Figure 2. *Casp8*$^{\Delta IEC}$ mice display non- to mild fibrotic inflammation. Mice were sacrificed at approximately 30 weeks. The experiment was repeated 2 times with similar results. (*A*) Comparison of the relative body weight gain starting from week 8 after birth of control, *Casp8*$^{\Delta ICE}$, *Mdr2*$^{-/-}$, and *Casp8*$^{\Delta ICE}$*xMdr2*$^{-/-}$ mice ($n \geq 7$ per group). (*B*) Representative *images* of colonic and liver cross sections stained with hematoxylin and eosin or Sirius Red. *Scale bar:* 500 μm. Liver cross sections were stained with an antibody against OmpC (*red*, *scale bar:* 25 μm). (*C*) Quantification of Sirius Red staining ($n \geq 6$). (*D*) Hepatic mRNA expression normalized to Gapdh ($n \geq 6$).

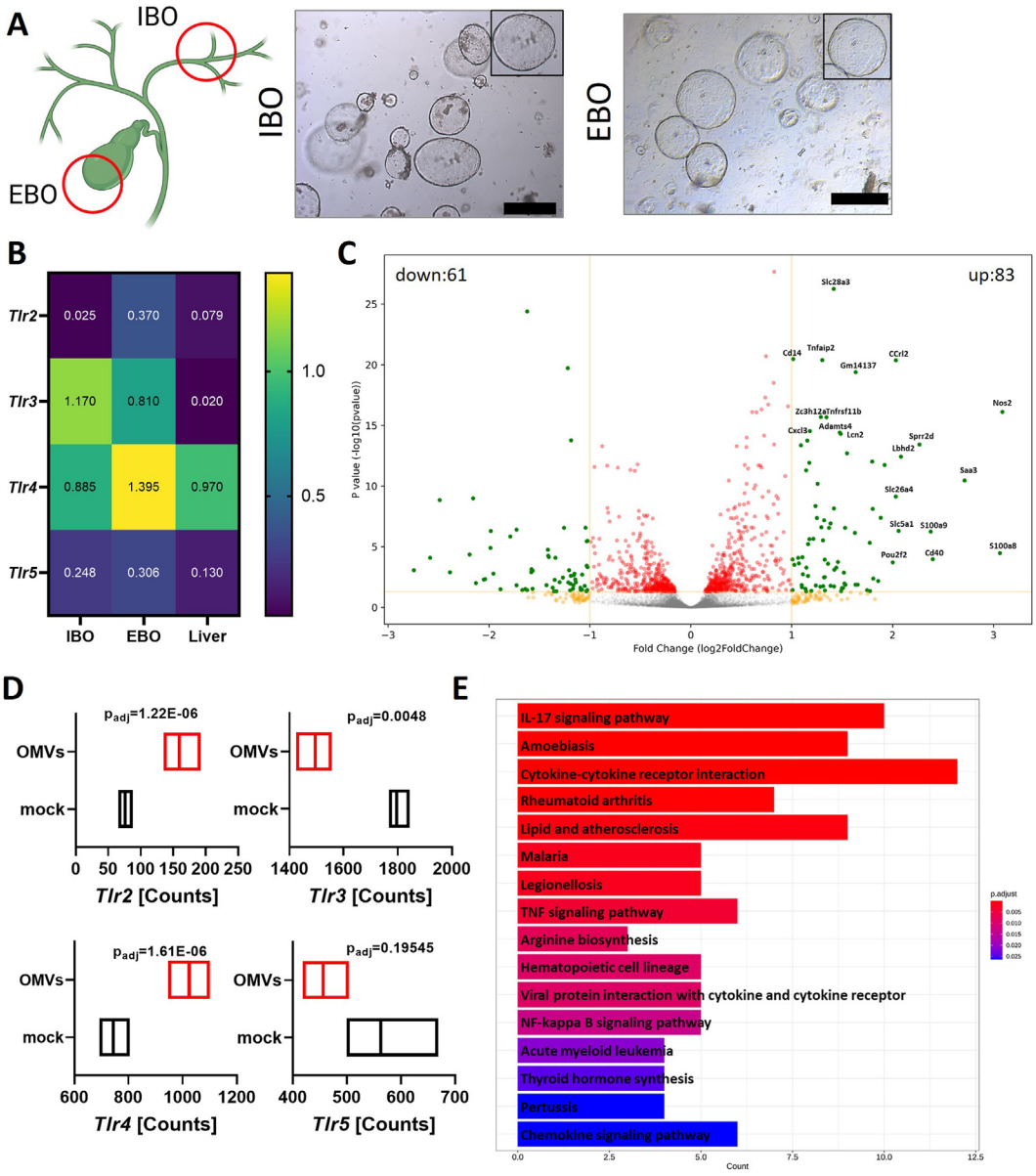

Supplementary Figure 3. OMVs trigger an inflammatory response via TLR signaling in IBOs. (*A*) Graphical depiction of organoid origin and representative *images* of murine IBOs and EBOs. *Scale bar:* 500 μm. (*B*) Analysis of gene transcription in organoids with relative mRNA expression normalized to Gapdh. Data are presented as medians. (*C–E*) Bulk RNA-sequencing data of murine IBO stimulated with OMVs derived from *E coli* BL21 (8.6×10^8 particles/mL) or mock treated for 8 hours. (*C*) *Volcano plot*. (*D*) Selected counts of indicated *Tlr*s and (*E*) KEGG pathway analysis.

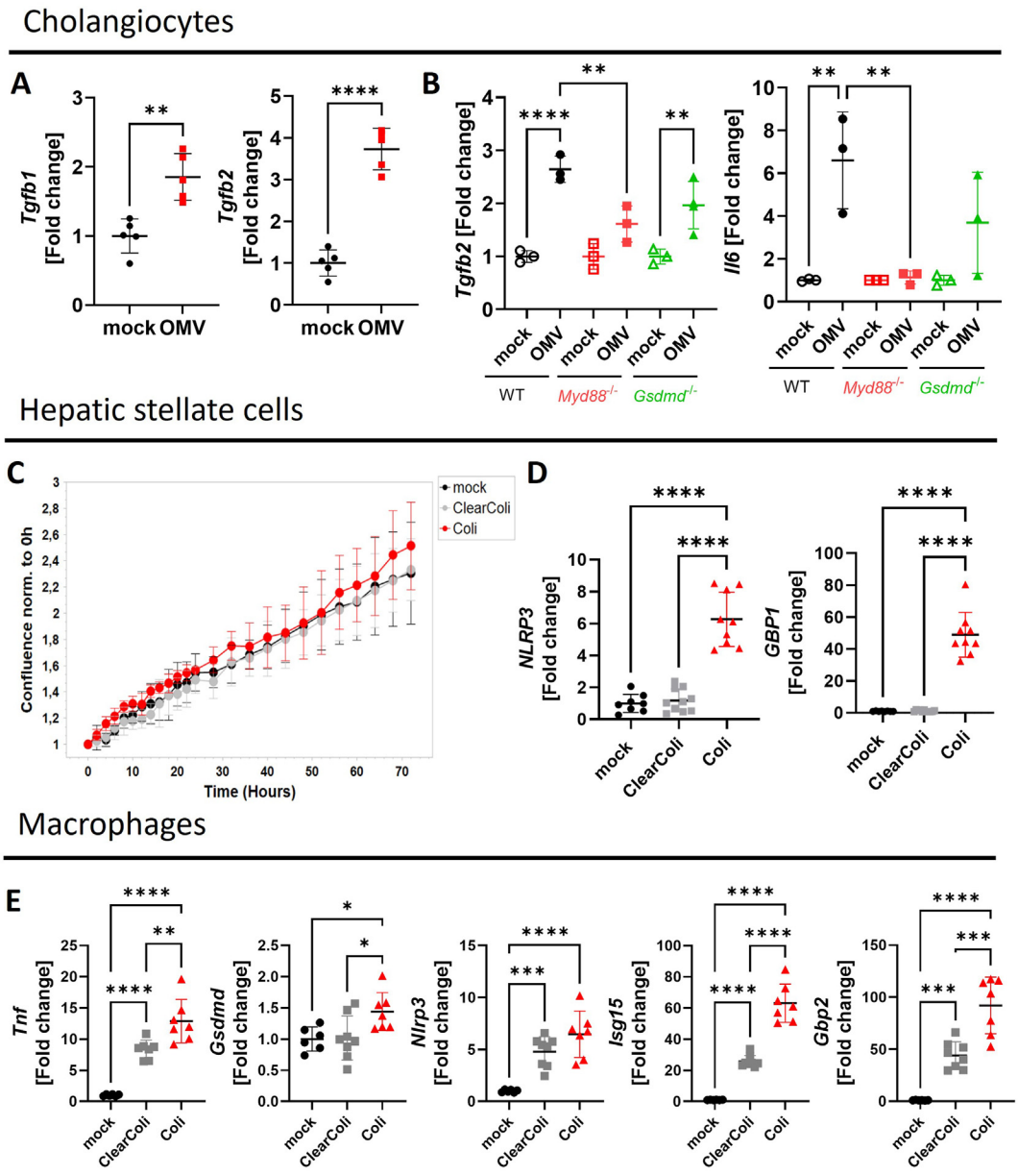

Supplementary Figure 4. OMVs orchestrate the host immune response by liver parenchymal cells. IBO generated from (*A*) control and (*B*) *Myd88*- and *Gsdmd*-deficient animals were exposed to OMVs (8.6×10^8 particles/mL) or mock treated for 8 hours. Gene expression normalized to *Rpl37a*. (*A*) n = 4 per group; statistical test: unpaired *t* test, (*B*) n = 3 per group; statistical test: ordinary 1-way analysis of variance (ANOVA) with Tukey's multiple comparisons test. WT, wild-type. (*C, D*) Human HSZ-B cells were stimulated with OMVs (1×10^9 particles/mL) or mock treated. (*C*) Cell growth was measured using the Incucyte SX5 and (*D*) mRNA expression (after 8 hours) normalized to *RPL37A*. n ≥ 8 per group; statistical test: ordinary 1-way ANOVA with Tukey's multiple comparisons test. (*E*) J774A.1 cells were stimulated with OMVs (1×10^9 particles/mL) or mock treated for 8 hours. mRNA expression normalized to *Rpl37a*. n ≥ 6 per group; statistical test: ordinary 1-way ANOVA with Tukey's multiple comparisons test. **P* < . 05; ***P* < .01; ****P* < .001; *****P* < .0001.

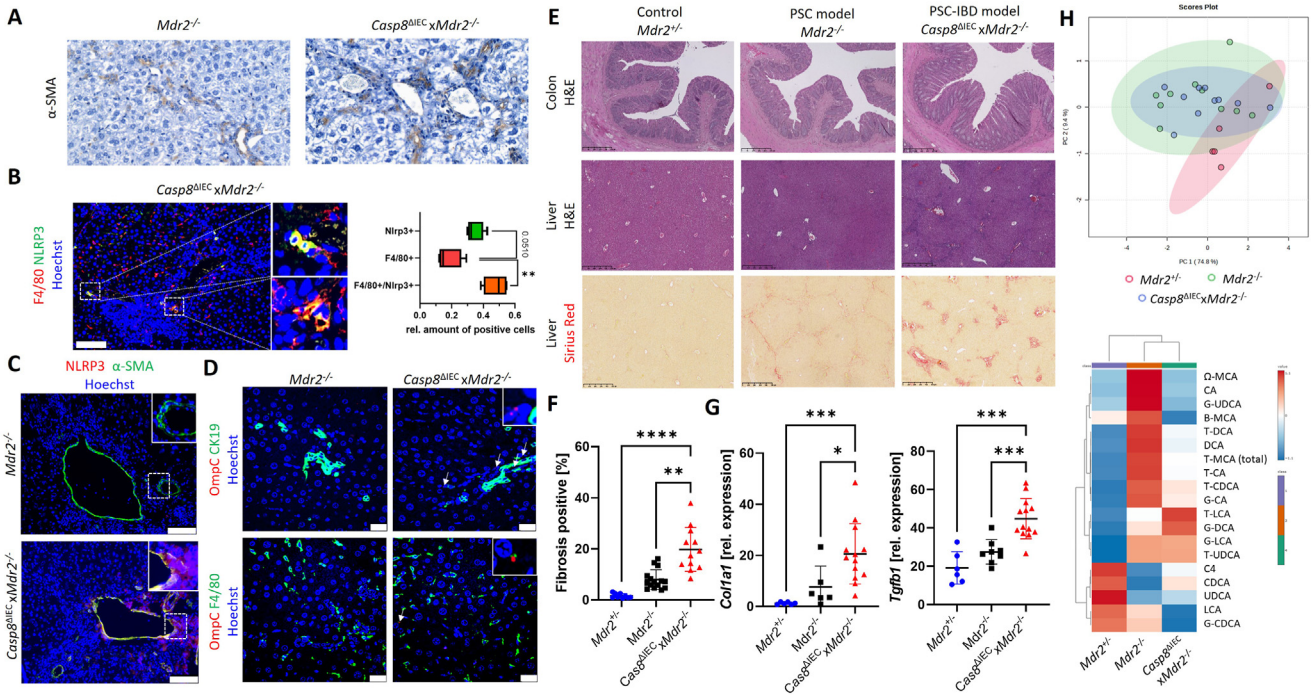

Supplementary Figure 5. NLRP3 expression by parenchymal cells in the liver of *Casp8*$^{\Delta IEC}$*xMdr2*$^{-/-}$ mice. Mice were sacrificed at approximately 30 weeks. The experiment was repeated 3 times with similar results. (*A*) Representative *images* of liver cross sections stained with an antibody against α–smooth muscle actin (α-SMA). (*B–D*) Representative *images* of liver cross sections immunohistochemically stained with antibodies against (*B*) NLRP3 (*green*) and F4/80 (*red*) and corresponding quantification (n = 4 per group; statistical test: Brown-Forsythe and Welch analysis of variance [ANOVA] with Dunnett's T3 multiple comparisons test [*scale bar:* 100 μm]) or (*C*) stained against NLRP3 (*red*) and α-SMA (*green*) (*scale bar:* 100 μm), (*D*) OmpC (*red*), and CK19 (*green*), or OmpC (*red*) and F4/80 (*green*). *Scale bar:* 25 μm. (*E*) Representative *images* of colon and liver cross sections stained with hematoxylin and eosin and Sirius Red. *Scale bar:* colon 250 μm, liver 500 μm. (*F*) Quantification of liver Sirius Red staining. (*G*) Gene transcription analysis of hepatic mRNA expression normalized to *Hprt*. Pooled data of independent experiments. n $\geq$ 6 per group; statistical test: Brown-Forsythe and Welch ANOVA with Dunnett's T3 multiple comparisons test. (*H*) Principal component analysis *plot* illustrating the distribution of serum bile acid profiles among *Mdr2*$^{+/-}$ (*red*, n = 5), *Mdr2*$^{-/-}$ (*green*, n = 10), and *Casp8*$^{\Delta IEC}$*xMdr2*$^{-/-}$ (*blue*, n = 10) mice. Each *point* represents an individual mouse, and clustering indicates similarities or differences in bile acid composition. *Heat map* showing relative abundance of individual bile acids in serum samples. *Color intensity* represents the level of each bile acid, with *red* indicating high abundance and *blue* indicating low abundance. Calculation of the total amount of primary vs secondary bile acids in serum samples.

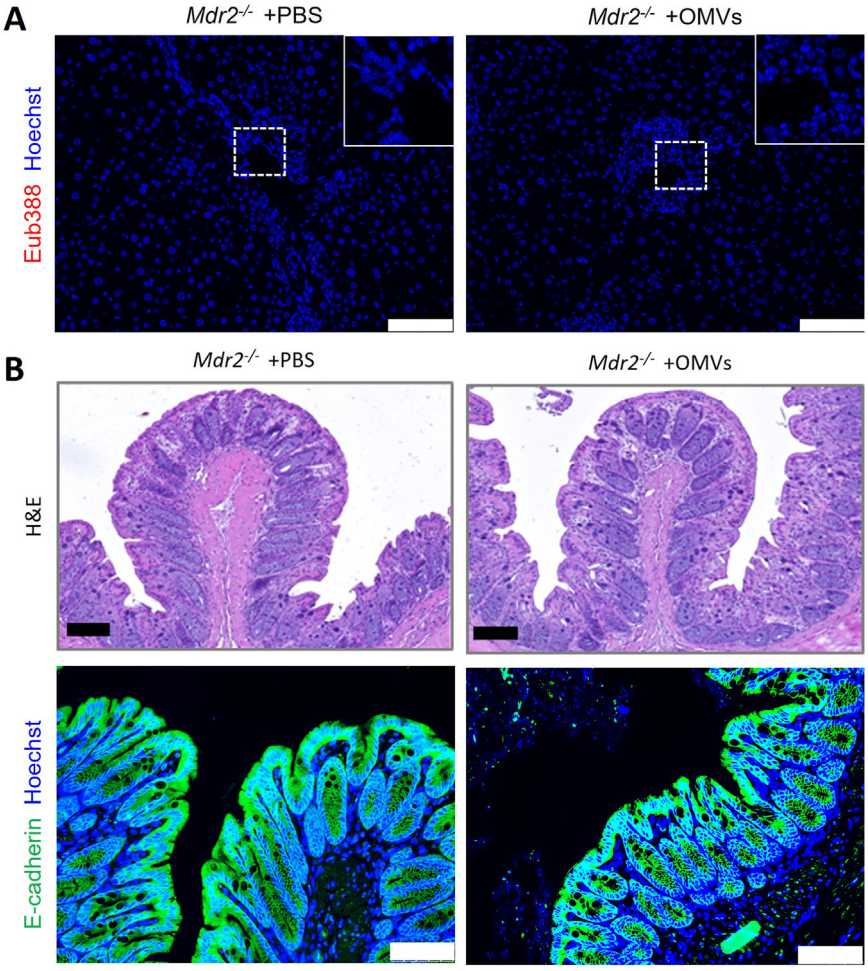

Supplementary Figure 6. Hepatic inflammation triggered by OMVs occurs independently of intestinal barrier impairment. *Mdr2*$^{-/-}$ mice (age approximately 15 weeks) were injected intraperitoneally with PBS (mock) or OMVs derived from pathogenic bacteria. Day 1: *K pneumonia* (1×10^9 particles in 100 μL PBS); day 2: *P mirabilis* (2×10^9 particles in 100 μL PBS); day 8: *P mirabilis* (1×10^9 particles in 100 μL PBS). Experiment was repeated 3 times with similar results and pooled data were displayed. *Mdr2*$^{-/-}$ +PBS n = 8; *Mdr2*$^{-/-}$ +OMVs n = 8. (*A*) Representative *images* of fluorescence in situ hybridization with a universal eubacterial probe (Eub388, *red*) in liver. *Scale bar:* 100 μm. (*B*) Hematoxylin and eosin-stained colon cross sections and representative *images* of colon cross sections immunohistochemically stained with an antibody against E-cadherin. *Scale bar:* 100 μm.

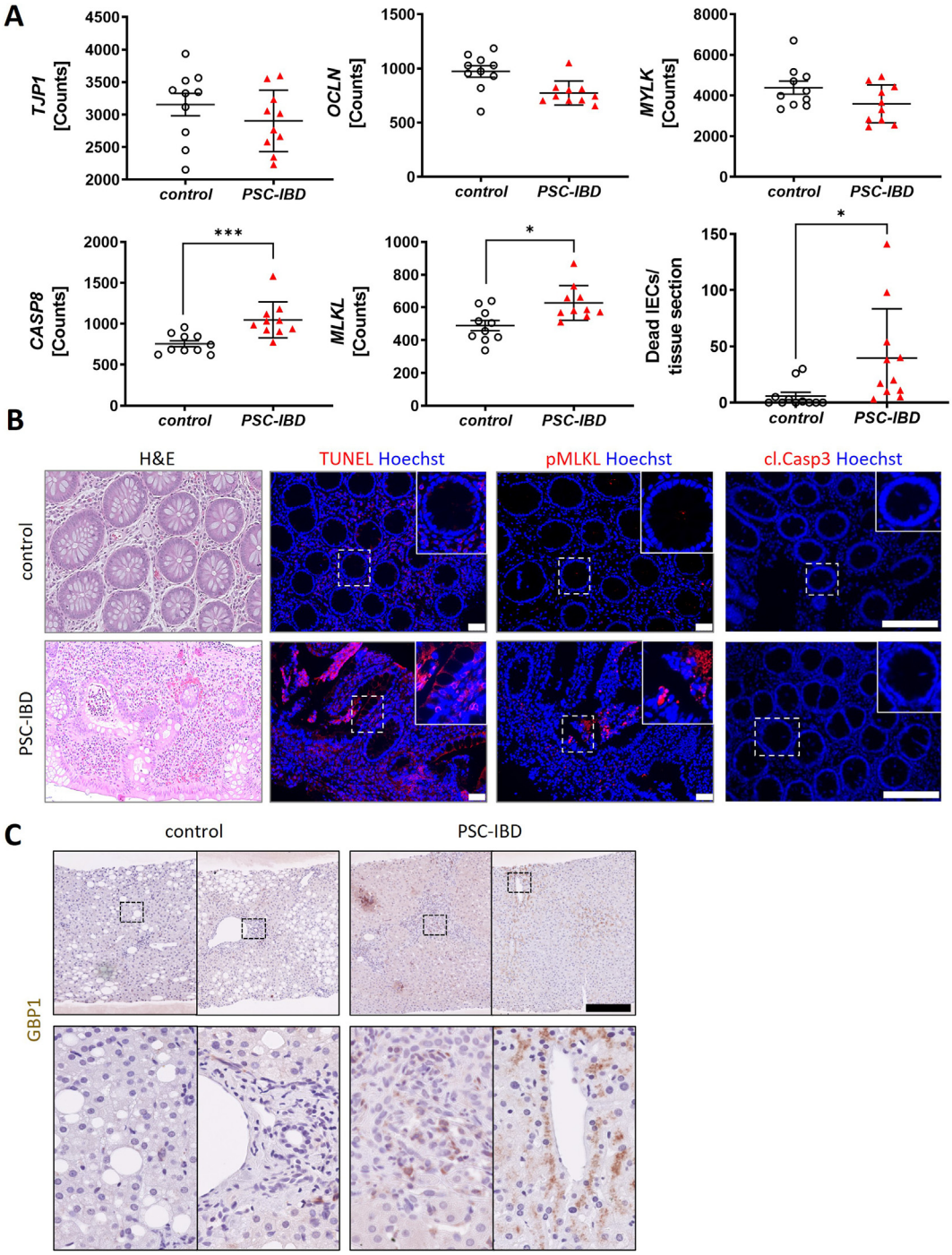

Supplementary Figure 7. Patients with PSC-IBD display a gene signature that points towards inflammatory cell death. (*A*) Bulk RNA-sequencing data of human colonic tissue. (*B*) Representative *images* of colon cross sections from human biopsies: hematoxylin and eosin-stained, terminal deoxynucleotidyl transferase–mediated deoxyuridine triphosphate nick-end labeling (TUNEL) assay (*red*, *scale bar:* 50 μm), or immunohistochemically stained with antibodies against pMLKL (*red*, *scale bar*: 50 μm) or activated caspase-3 (cl. Casp3, *red, scale bar:* 130 μm). (*C*) Representative *images* of liver cross sections from human biopsy stained with an antibody against GBP1. *Scale bar:* 250 μm.

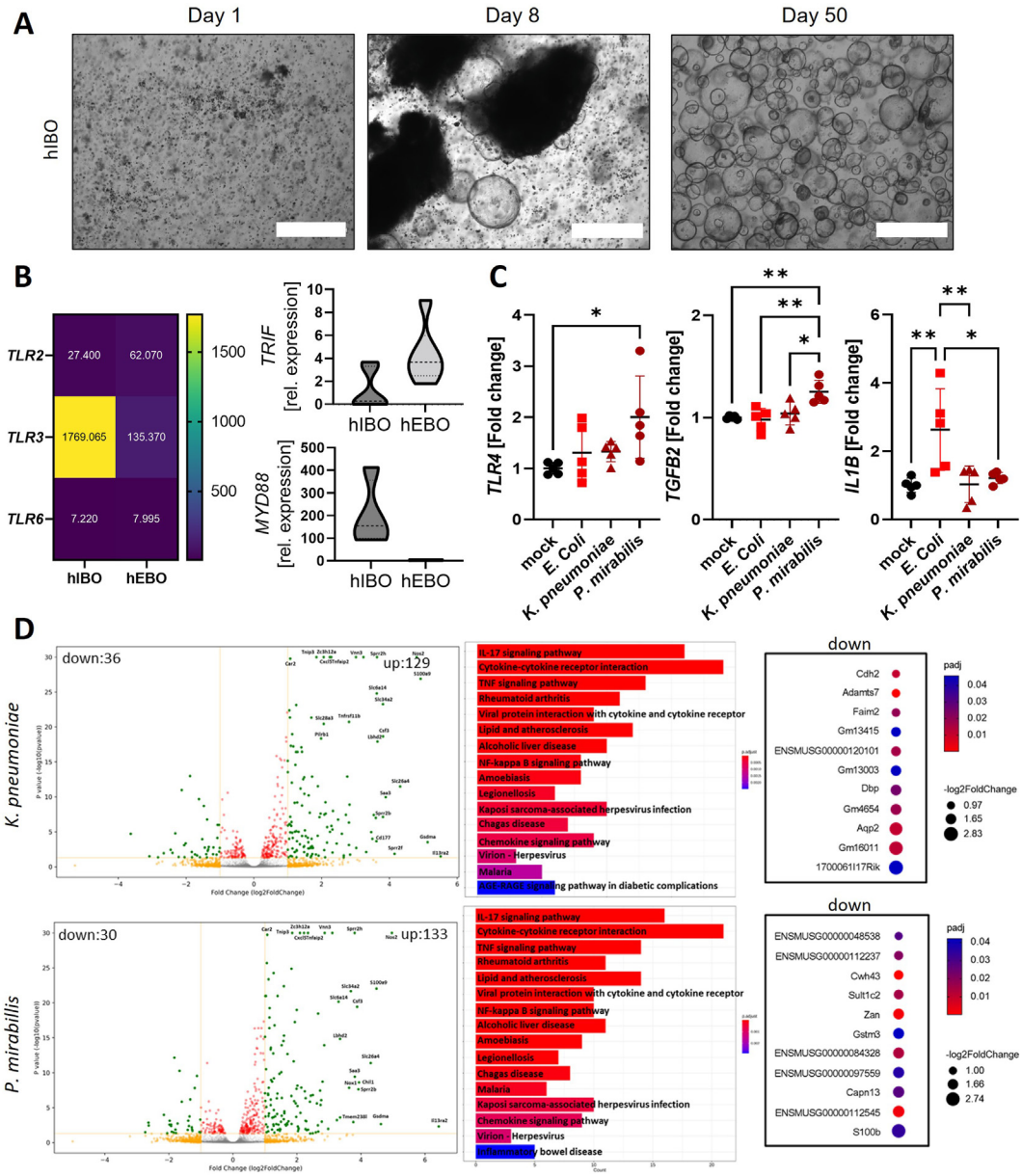

Supplementary Figure 8. Gut pathobionts induce a pro-inflammatory fingerprint in ductal organoids. (*A*) Representative *images* of hIBOs. *Scale bar:* 800 μm. (*B*) Gene transcription analysis of organoid mRNA expression normalized to GAPDH. Data represented as *heat map* with median or as *violin plot*. n = 6 per group. (*C*) Human IBO stimulated with OMVs (8.6×10^8 particles/mL) mock treated for 8 hours. Gene transcription analysis of organoid mRNA expression normalized to *RPL37A*. n = 5 per group; statistical test: ordinary 1-way analysis of variance with Tukey's multiple comparisons test. *$P < .05$; **$P < .01$. (*D*) Bulk RNA-sequencing data from murine IBOs stimulated with OMVs (8.6×10^8 particles/mL) treated for 8 hours. Data analyzed as OMVs vs mock. *Volcano plot*, KEGG pathway analysis and top down-regulated genes.

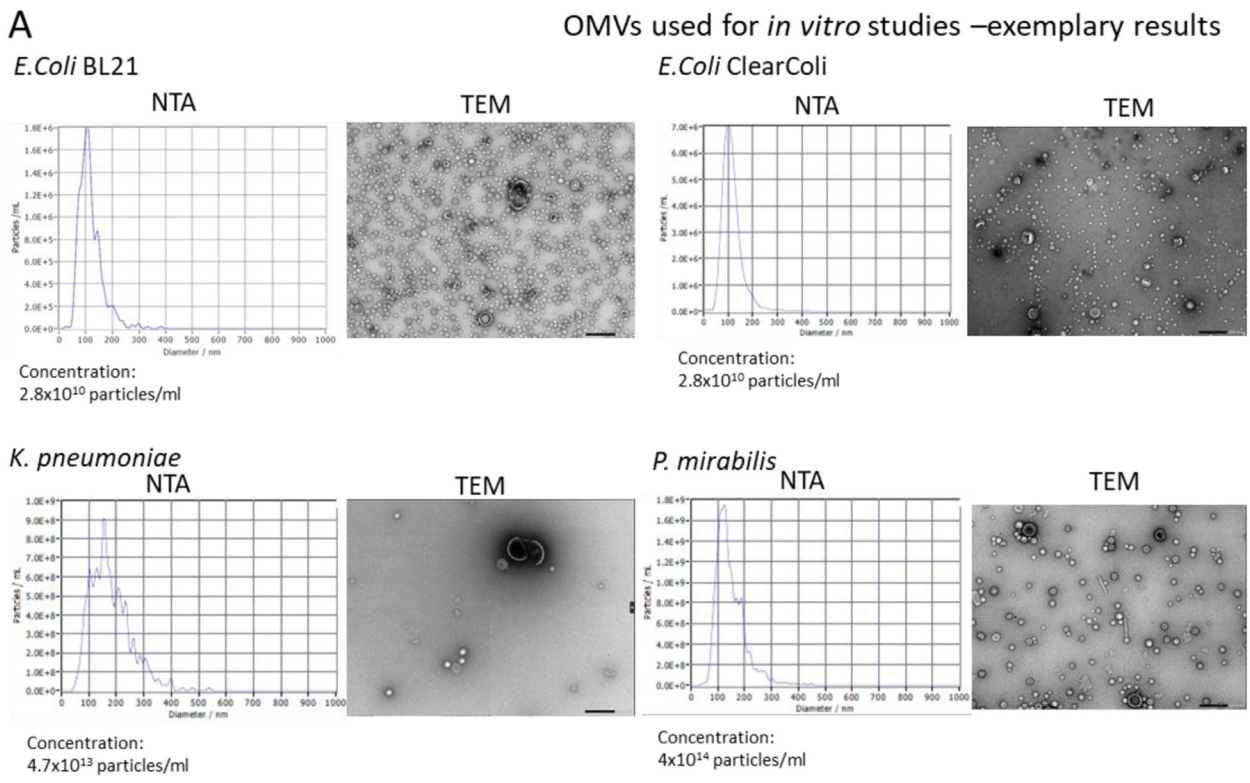

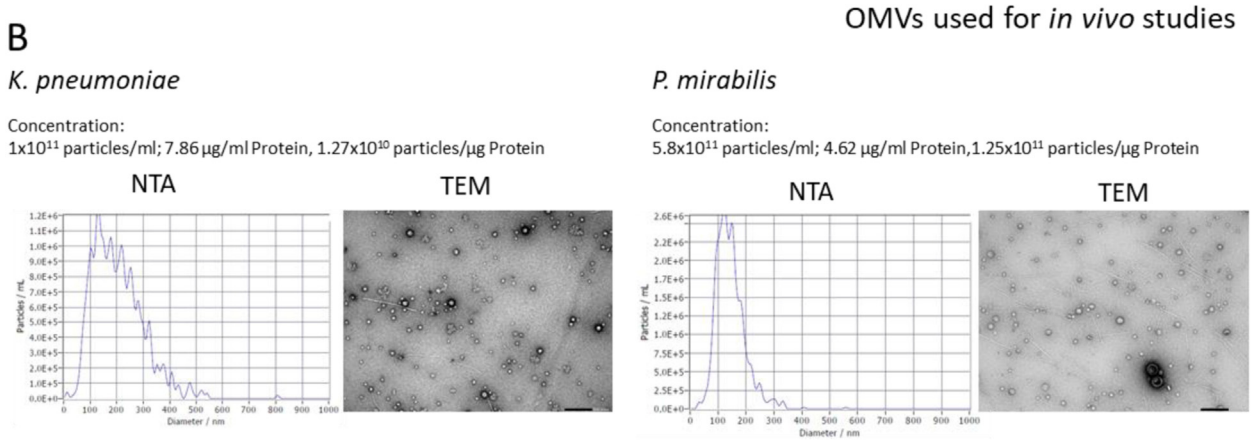

	clone 9	clone 10	clone 11	clone 12
chromosome	5244609 bp	5249776 bp	5266927 bp	5368224 bp
plasmid(s)	none	181794 bp	142151 bp, 138199 bp, 137916 bp	296625 bp, 256375 bp
AMR	oqxA, oqxB, fosA6, blaSHV-11	oqxA, oqxB19, fosA6, blaSHV-1	oqxA, oqxB, fosA6, blaSHV-11, pmrB_R256G, ramr_A19V	oqxA, oqxB, fosA6, blaSHV-11, pmrB_R256G
sequence type	ST2440	ST397	ST37	ST12
K locus	KL62	KL158	KL12	KL122
MLST	gapA_3, infB_5, mdh_95, pgi_1, phoE_7, rpoB_1, tonB_12	gapA_2, infB_1, mdh_1, pgi_1, phoE_21, rpoB_44, tonB_9	gapA_2, infB_9, mdh_2, pgi_1, phoE_13, rpoB_1, tonB_16	gapA_6, infB_3, mdh_1, pgi_1, phoE_12, rpoB_1, tonB_4
O locus	O1/O2v1	O1/O2v1	OL103	O1/O2v2

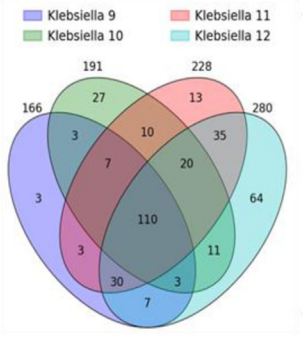

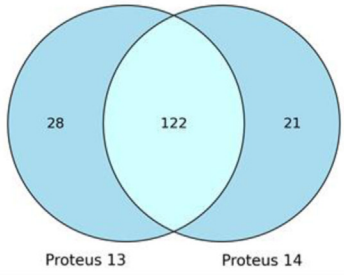

Supplementary Figure 9. Supplementary information for used OMVs. Characterization of used OMVs for (*A*) in vitro and (*B*) in vivo. Representative nanoparticle tracking analysis (NTA) and transmission electron microscopy (TEM) *pictures* of isolated OMVs and key bacterial features of the different *Klebsiella* clones identified through genome sequencing, as well as *Venn diagrams* illustrating the comparative protein function analyses of OMVs derived from distinct bacterial strains. Each *circle* represents the functional protein categories of OMVs isolated from a specific bacterial strain, with the overlapping regions indicating shared proteins between the strains.

Supplementary Table 2. Quantitative Polymerase Chain Reaction Primer

Primer	Catalog number or sequence	Company
mM_Casp1_1	QT00199458	Qiagen
mM_Casp4_1	QT00096117	Qiagen
mM_Casp8_1	QT00171437	Qiagen
mM_Casp11	Fwd: tcctttaatttcagtacattgctttg Rev: tgaggctttttctcatggct	biomers.net
mM_Cd14	Fwd: ctagtcggattctattcggagc Rev: agacaggtctaaggtggagagg	biomers.net
mM_Cd68_1	QT00254051	Qiagen
mM_Col1a1_1	QT00162204	Qiagen
mM_Ctgf_1	QT00096131	Qiagen
mM_Emr1_1	QT00099617	Qiagen
mM_Gapdh	Fwd: tcaccaccatggagaaggc Rev: gctaagcagttggtggtgca	biomers.net
mM_Gbp2_1	QT00106050	Qiagen
mM_Gsdmd	QT00107247	Qiagen
mM_Gsdmd	Fwd: ccgggttgagcagacaatag Rev: accactttctcaaaggccg	biomers.net
mM_Hprt_1	QT00166768	Qiagen
mM_Ifit_1	QT01161286	Qiagen
mM_Il1b_2	QT01048355	Qiagen
mM_Il6	QT00098875	Qiagen
mM_Isg15_1	QT00322749	Qiagen
mM_Mki67_1	QT00247667	Qiagen
mM_Mlkl_1	QT01069285	Qiagen
mM_Nlrp3	Fwd: aagtaaggccggaattcacc Rev: aaaatgccttgggagactca	biomers.net
mM_Nos2_1	QT00100275	
mM_Rpl37a	Fwd: tgtggttcctgcatgaaaaca Rev: gtgactgcgaggtggtgttgtag	biomers.net
mM_Tgfb1_1	QT00145250	Qiagen
mM_Tgfb2_1	QT00106806	Qiagen
mM_Tnf_1	QT00104006	Qiagen
mM_Tlr2_1	QT00129752	Qiagen
mM_Tlr3_1	QT00122983	Qiagen
mM_Tlr4_1	QT00259042	Qiagen
mM_Tlr5_2	QT02328221	Qiagen
Hs_GAPDH_1	QT00079247	Qiagen
Hs_GBP1_1	QT00011641	Qiagen
Hs_IL1B_1	QT00021385	Qiagen
Hs_MYD88_1	QT00203490	Qiagen
Hs_NLRP3_1	QT00029771	Qiagen
Hs_RPL37A	Fwd: tgtggttcctgcatgaagaca Rev: gtgacagcggaagtggtattgtac	biomers.net
Hs_TGFB2_1	QT00025718	Qiagen
Hs_TICAM_1	QT00201614	Qiagen
Hs_TLR2_1	QT00236131	Qiagen
Hs_TLR3_1	QT00007714	Qiagen
Hs_TLR4_2	QT01670123	Qiagen
Hs_TLR6_1	QT00216272	Qiagen

Supplementary Table 3. Products for Immunohistochemistry

Antibody/kit	Catalog no.	Company
Alexa Fluor 647 anti-mouse CD31 antibody	102516	BioLegend
Anti–α-smooth muscle actin antibody	Ab5694	Abcam
Anti–α-smooth muscle actin antibody	Ab32575	Abcam
Anti-cytokeratin 19 antibody	ab52625	Abcam
Anti-cytokeratin 19 antibody, clone TROMA-3	MABT913	Sigma-Aldrich
Anti-NLRP3/NALP3	AG-20-B-0014-C100	Adipogen
Biotin goat anti-rat immunoglobulin	554014	BD Bioscience
CD45R (B220) monoclonal antibody	14-0451-82	Invitrogen
Cleaved caspase-3 (Asp175) antibody	CS9661	Cell Signaling Technology
Donkey anti-rabbit IgG (H+L) highly cross-adsorbed secondary antibody, Alexa Fluor 488	A-21206	Invitrogen
Eub338	5′-GCT GCC TCC CGT AGG AGT-3′, containing a Cy3-3 modification	biomers.net
F4/80 monoclonal antibody	14-4801-85	eBioscience
Fluorescein isothiocyanate mouse anti–E-cadherin	612130	eBioscience
Goat IgG anti-rabbit IgG (H+L)-biotin	111-065-144	Dianova
GSDMDC1 antibody (H-11)	sc-393581	Santa Cruz Biotechnology
Hoechst 33342	H3570	Invitrogen
Horse anti-mouse IgG antibody (H+L), biotinylated	BA2000	Vector
In situ cell death detection kit	11684795910	Roche
M.O.M.-Kit	FMK-2201	Vector
MLKL [pThr357] antibody	MAB91871	Novus
ompC antibody	orb308739	Biorbyt
Purified rat anti-mouse CD4	553043	BD Bioscience
Rat anti-mouse F4/80	MCA497GA	Bio-Rad
Recombinant anti–interleukin-1β antibody	Ab216995	Abcam
Recombinant anti-Ki67 antibody	ab16667	Abcam
Streptavidin DyLight 550	84542	Thermofisher
Streptavidin DyLight 649	405224	Biolegend
TSA Fluorescence System cyanine 3/fluorescein	NEL704A001KT / NEL701A001KT	Perkin Elmer